

REVIEW ARTICLE OPEN

A review: applications of the phase field method in predicting microstructure and property evolution of irradiated nuclear materials

Yulan Li¹, Shenyang Hu¹, Xin Sun¹ and Marius Stan²

Complex microstructure changes occur in nuclear fuel and structural materials due to the extreme environments of intense irradiation and high temperature. This paper evaluates the role of the phase field method in predicting the microstructure evolution of irradiated nuclear materials and the impact on their mechanical, thermal, and magnetic properties. The paper starts with an overview of the important physical mechanisms of defect evolution and the significant gaps in simulating microstructure evolution in irradiated nuclear materials. Then, the phase field method is introduced as a powerful and predictive tool and its applications to microstructure and property evolution in irradiated nuclear materials are reviewed. The review shows that (1) Phase field models can correctly describe important phenomena such as spatial-dependent generation, migration, and recombination of defects, radiation-induced dissolution, the Soret effect, strong interfacial energy anisotropy, and elastic interaction; (2) The phase field method can qualitatively and quantitatively simulate two-dimensional and three-dimensional microstructure evolution, including radiation-induced segregation, second phase nucleation, void migration, void and gas bubble superlattice formation, interstitial loop evolution, hydrate formation, and grain growth, and (3) The Phase field method correctly predicts the relationships between microstructures and properties. The final section is dedicated to a discussion of the strengths and limitations of the phase field method, as applied to irradiation effects in nuclear materials.

npj Computational Materials (2017)3:16; doi:10.1038/s41524-017-0018-y

INTRODUCTION

High energy particle (such as neutron, ion, and electron) radiation can create major changes in the shape and thermo-mechanical properties of nuclear fuels and structural components of nuclear reactors. These changes are caused by radiation-induced evolution of compositions and microstructures. The main effects of radiation on reactor materials are: (1) dimensional change associated with gas bubble swelling, void swelling, grain growth, and creep;^{1–5} (2) loss of ductility and increase in ductile-brittle transition temperature (DBTT) due to the formation of second-phase precipitates, self-interstitial atomic (SIA) loops, and dislocation networks;^{6, 7} (3) oxidation and corrosion accelerated by high temperature, fission products, and radiation damage;^{8–10} and (4) local and bulk changes in chemical composition, including irradiation-enhanced segregation of alloy components and phase separation.^{11–17} Figure 1 shows typical microstructures observed in irradiated materials.^{9, 18–21} The radiation-induced heterogeneity of the microstructures depends on the initial phase and defect structure of the fresh (non-irradiated) materials and on the type and severity of the radiation environment. Fundamental understanding of heterogeneous three-dimensional microstructure evolution is crucial to the development of advanced radiation tolerant materials that can significantly improve the life extension of current reactor fleet and impact advanced reactor designs.

Over the past three decades, molecular dynamics (MD) methods have been extensively used to study the thermodynamic and kinetic properties, generation, and interaction (annihilation,

absorption, and emission) of irradiation defects as well as the physical mechanisms of defect evolution.^{22–26} The results of classical MD simulations can be enhanced by capturing quantum effects. To that end, density functional theory (DFT) calculations have been increasingly employed to evaluate thermodynamic and kinetics properties of irradiation defects in alloys and nuclear fuels.^{27–30} In addition, methods of kinetic Monte Carlo (kMC),^{31–34} Object kinetic Monte Carlo (OkMC),^{35–37} cluster dynamics^{38, 39} and rate theory^{36, 37, 40–42} have been used extensively to study long-time evolutions of defects and defect clusters in radiation environments. It was demonstrated that atomistic simulations can provide the thermodynamic and kinetics properties of radiation-induced defects and defect clusters, while kMC and rate theory can predict defect cluster evolution. However, there are significant challenges in using these methods to predict the three-dimensional (3-D) mesoscale microstructure evolution—as shown in Fig. 1—and the subsequent impact on thermo-mechanical properties such as thermal conductivity degradation, hardening, and DBTT. To understand material property degradation, one of the key issues is to develop the modeling capability to predict the microstructure evolution, the relationship between microstructure and properties, and the impact of microstructural changes on the material response to applied fields.

Microstructure evolution in irradiated nuclear materials is a complex process that covers large time and length scales, ranging from individual atomic events, such as point defect generation during radiation cascades on the scale of femtoseconds and

¹Pacific Northwest National Laboratory, 902 Battelle Boulevard, Richland, WA 99352, USA and ²Argonne National Laboratory, 9700 South Cass Avenue, Lemont, IL 60439, USA
Correspondence: Shenyang Hu (shenyang.hu@pnnl.gov)

Received: 12 December 2016 Revised: 9 March 2017 Accepted: 21 March 2017

Published online: 14 April 2017

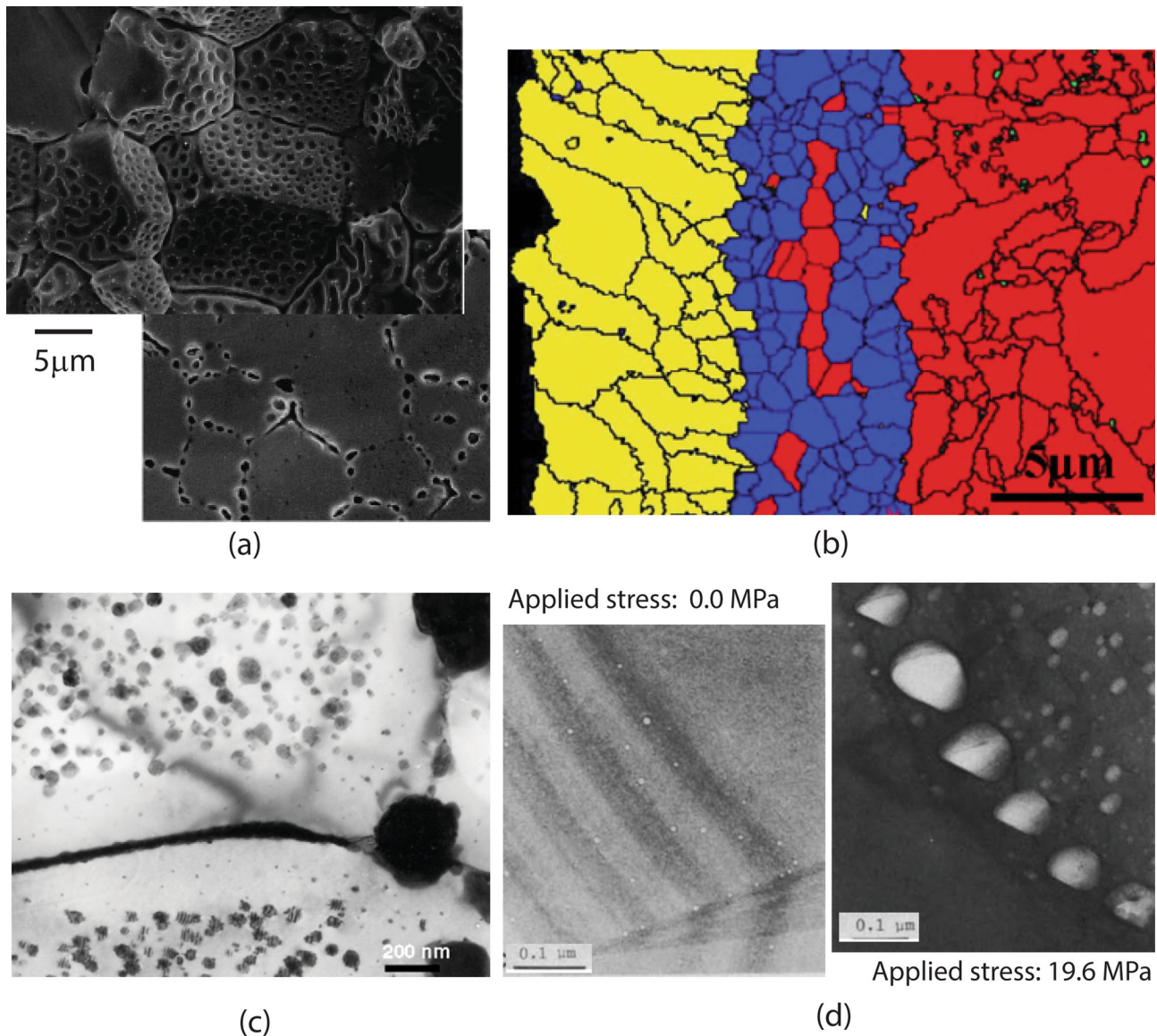


Fig. 1 **a** Scanning electron microscope (SEM) image of gas bubble structure in UO_2 (ref. 21); **b** Cross-section electron backscatter diffraction (EBSD) image of oxide layers on ferritic/martensitic (F/M) steels that exposed at 500 °C to low oxygen concentration (25 parts-per-billion or ppb) supercritical water (SCW) for 505 h. Yellow: Magnetite Fe_3O_4 , Blue: Spinel $(\text{Fe,Cr})_3\text{O}_4$, Red: base metal F/M (ref. 9); Bright-field image of zone denuded of phase precipitate in EP-450 (ref. 19); **d** Effect of tensile stress on helium gas bubble structures in Fe-17wt%Cr-17wt%Ni after annealing at 1023 K for 60 h (ref. 20)

nanometers, to long-term diffusion and grain size and shape evolution on the scale of years and micrometers.^{13, 43–45} Microstructure changes under radiation often involve coupled material processes such as: generation of defects associated with neutron radiation and transmutation reaction; diffusion and accumulation of vacancies, SIAs, their clusters, solute atoms, and fission products; and phase transition such as radiation-induced dissolution and the formation of second-phase particles, voids, gas bubbles, and SIA loops. Furthermore, under radiation, defects are produced randomly in time and space. The spatial and time dependence of defect generation coupled with long-range interaction with structural defects such as grain boundaries (GBs) introduces heterogeneity in chemistry and microstructure, adding to the challenges of microstructure evolution modeling.

The phase field (PF) method, as a powerful mesoscale simulation tool, has been successfully applied to predict complex 3-D microstructure evolution kinetics in important materials processes, such as solidification and melting, ferroelectric and

ferromagnetic phase transition, phase-separation and precipitation, martensitic transition, dislocation dynamics, twinning and detwinning, and electrochemical processes. The PF method is based on the fundamental thermodynamic laws, the kinetics of defects in the system under examination, and the understanding of the mechanisms behind the material processes. It has multiple advantages that include: (1) no prior assumption on microstructure morphology, (2) no need to explicitly track the location of interfaces, (3) multi-dimensional (two-dimensional (2-D), 3-D), computationally efficient representation of multiple material processes with short- and long-range interactions, and (4) multi-dimensional (2-D, 3-D), computationally efficient representation of inhomogeneous and anisotropic properties of defects and materials. Applications of the PF method in predicting microstructure evolution in solidification and solid state phase transition have been reviewed in several articles.^{46–53}

During the past decade, the PF approach has been applied to study microstructure evolutions in irradiated nuclear materials

such as gas bubble evolution in nuclear fuels,^{54–62} void formation and evolution,^{63–73} void and gas bubble lattice formation,^{62, 74} void migration under temperature gradient,^{75–77} SIA loop growth kinetics,^{78–80} precipitation,^{81–90} grain growth and recrystallization.^{91–95} Millett and Tonks reviewed the application of PF models in predicting void and gas bubble evolution.⁹⁶ The PF method also has been used to study the effect of microstructures on material property degradation including radiation-induced void and gas bubble swelling.^{55, 65, 91, 97–108} Although the PF method has been used to simulate a large number of radiation-induced microstructure evolution phenomena, direct validation of PF models published in the literatures is difficult because most current PF models only addressed one or a couple of multiple microstructures in irradiated materials. Furthermore, there was very limited experimental data for the validation of specific microstructures and processes. However, the method has demonstrated its ability to describe complex material processes and the associated 3-D microstructural changes. This work aims to review the various applications of PF method in predicting microstructure evolution of irradiated nuclear materials and discuss the challenges and areas of potential rapid improvement. The paper is organized as follows: the PF approach is introduced in the next section. Then, the reviews of the important applications of the PF approach in modeling microstructure evolution in irradiated nuclear materials and the application of the PF method in predicting the relationship between microstructure and materials properties and material response are given in the followed 2 sections, respectively. The final section offers conclusions based on the state-of-the-art PF simulations while answering important questions: “What does the PF method provide to the understanding of radiation effects, that other methods cannot?”, “How can a free energy minimization method describe irradiation effects?”, “Is the PF method qualitative or quantitative?” and “Is the PF method computationally efficient?”

INTRODUCTION OF THE PF METHOD

The irradiated material's microstructure is inherently inhomogeneous in composition and features.⁴⁶ In the PF method, two sets of field variables are used to describe the microstructure. One is the *concentration field* that describes the spatial distributions of species of interest, including impurity, fission gas atoms, vacancies, SIAs, etc. The other is the *order parameter field*, which describes the spatial distributions of microstructural features, such as crystal structures, crystal orientations, voids, dislocation loops, gas bubbles, and/or ferromagnetic domains. In the assumption of a chemically closed system, the concentration field is conserved while the order parameter field is not. All of the field variables in PF models change smoothly across the interface. Therefore, the interfaces are diffuse (not sharp). The diffuse interface does not need to explicitly track the exact location of interfaces, and can eliminate the singularity of fields at the interface such as the stress fields. This key characteristic of the PF method considerably improves the efficiency of the computation compared to sharp interface microstructure evolution methods, for example, the level set approach,¹⁰⁹ which needs to track the location of interfaces. As discussed in the previous section, microstructure evolution in irradiated nuclear materials usually involves multi-component diffusion and multi-phase transition. Thus, the concentration field is represented by a concentration vector $\mathbf{c} = \{c_1(\mathbf{x}, t), c_2(\mathbf{x}, t), \dots, c_M(\mathbf{x}, t)\}$, and the order parameter field is represented by an order parameter vector $\boldsymbol{\eta} = \{\eta_1(\mathbf{x}, t), \eta_2(\mathbf{x}, t), \dots, \eta_N(\mathbf{x}, t)\}$, where M and N are the total number of species and phases and/or structures of interest. Here $\mathbf{x} = (x_1, x_2, x_3)$ is the spatial coordinate, and t is the time. The total free energy of the system expressed in terms of the

PF variables \mathbf{c} and $\boldsymbol{\eta}$ is given by:

$$F = \int_V [f_{\text{ch}}(\mathbf{c}; \boldsymbol{\eta}) + f_{\text{grad}}(\mathbf{c}; \boldsymbol{\eta}) + f_{\text{lr}}(\mathbf{c}; \boldsymbol{\eta})] dV, \quad (1)$$

where V is the volume of the considered system; f_{ch} is the chemical free energy density; f_{grad} is the gradient energy density associated with the interfacial energy and can be expressed generally as

$$f_{\text{grad}}(\mathbf{c}; \boldsymbol{\eta}) = \sum_m \frac{1}{2} \kappa_{cm} (\nabla c_m)^2 + \sum_n \frac{1}{2} \kappa_{\eta n} (\nabla \eta_n)^2, \quad (2)$$

where $\nabla = \frac{\partial}{\partial x_1} + \frac{\partial}{\partial x_2} + \frac{\partial}{\partial x_3}$, $\kappa_{cm} (m = 1, \dots, M)$ and $\kappa_{\eta n} (n = 1, \dots, N)$ are the gradient coefficients for concentration c_m and order parameter η_n respectively. The gradient terms result in diffuse interfaces in PF modeling. In this formulation, f_{lr} is the long-range interaction energy density that may include elastic energy, magneto-static energy, etc. The evolution of $\mathbf{c} = \{c_1, c_2, \dots, c_M\}$ and $\boldsymbol{\eta} = \{\eta_1, \eta_2, \dots, \eta_N\}$ follows the time-dependent Cahn-Hilliard¹¹⁰ and Ginzburg-Landau or Allen-Cahn equations,¹¹¹ respectively:

$$\frac{\partial c_i}{\partial t} = \nabla \cdot \sum_j \left(M_{ij} \nabla \frac{\delta F}{\delta c_j} \right) + \xi_i + \dot{g}_i + \dot{\gamma}_i + \dot{S}_i, \quad (i = 1, 2, \dots, M), \quad (3)$$

$$\frac{\partial \eta_\rho}{\partial t} = -L_\rho \frac{\delta F}{\delta \eta_\rho} + \xi_\rho, \quad (\rho = 1, 2, \dots, N), \quad (4)$$

where M_{ij} is the chemical mobility tensor, L_ρ is the interface mobility, ξ_i and ξ_ρ are the thermal fluctuations. The last three terms in Eq. (3) describe the rates of generation, reaction, and sink of species i , respectively, in an irradiation environment. For vacancies and interstitials, the generation rate \dot{g}_i can be calculated by $\dot{g}_i = G_{\text{NRT}}(1 - \Omega_R)(1 - \theta_i)$, where G_{NRT} is the total production rate of displacements per atom (dpa), which can be calculated using the model proposed by Norgett, Robinson, and Torrens, known as the NRT standard.¹¹² Here Ω_R is the fraction of defects recombined in cascades relative to the NRT standard value, and θ_i is the fraction of clustered vacancies ($i = \text{vac}$) or SIAs ($i = \text{int}$). For fission gas ($i = \text{gas}$), the generation rate can be calculated by $\dot{g}_{\text{gas}} = \bar{f} Y_{\text{gas}}$, where \bar{f} is the fission rate and Y_{gas} is the yield of gas atoms per fission. $\dot{\gamma}_i$ is the reaction rate, which is proportional to diffusivity and concentrations of the interacted species. For example, by considering the recombination of vacancies and interstitials, $\dot{\gamma}_i = \mu_R D_{\text{int}} c_{\text{vac}} c_{\text{int}}$ where μ_R is the recombination coefficient, D_{int} is the diffusion coefficient of interstitials; c_{vac} and c_{int} are the concentrations of vacancies and interstitials, respectively. \dot{S}_i is the sink rate. For vacancies and interstitials, it can be calculated as $\dot{S}_i = -k_i^2 D_i c_i$, ($i = \text{vac}, \text{int}$), where k_i^2 is the sink strength. There are a number of publications devoted to the derivation of sink strengths. The parameters, \dot{g}_i , $\dot{\gamma}_i$, and \dot{S}_i , could be described by the expressions derived from the rate theory.^{112, 113} It is important to note that the sink strength and reaction rates can be described by both the mean field method and the rate theory. For instance, sink strength depends on the interaction energy between the sink and defects while reaction rate depends on the reaction energy barriers. Once the interaction energy and reaction energy barriers are known, e.g., calculated from atomistic simulations, the interaction energy can be added to the local chemical free energy while the reaction energy barrier can be used to calculate the local reaction rate. Thus, inhomogeneous and time evolving sinks and reaction rate can be taken into account in the PF model if the sink is described by PF variables.⁶⁴ Recently, Hochrainer and El-Azab developed a sharp interface model in the thermodynamic and kinetic framework to study the defect reaction kinetics at interface and void growth kinetics.⁷³ The sharp interface model can be used to numerically validate the PF models and determine model parameters of interface reaction

in PF models. For the defect generation, it is straightforward to introduce a spatial-dependent generation of defects into PF models based on the MD simulations of cascades.¹¹⁴

Equations (1–4) present a general description of a multi-component, multi-phase PF model. The PF models have previously been classified into types A, B, and C^{115, 116} analogous to the well-known classification of the dynamic critical phenomena models in condensed-matter physics by Hohenberg and Halperin.¹¹⁷ For a system with multicomponent and multiphase, one can usually compute the free energies of different phases from thermodynamic calculations such as CALculation of Phase Diagrams (CALPHAD). In the CALPHAD method, the free energies of different phases are described as functions of concentrations, temperature, and pressure. The functions may have different forms ranging from ideal or regular solutions to multiple sublattice thermodynamic models. Therefore, the manner in which the total free energy functional is constructed with the known chemical free energies and PF variables will determine the evolution equations of the PF model. For these reasons, we categorize the PF models into four types according to the free energy formulation:

Model 1 (CH): The free energy and microstructure are completely described by the concentration field $\mathbf{c} = \{c_1, c_2, \dots, c_M\}$. The total free energy is calculated by $F = \int_V [f_{\text{ch}}(\mathbf{c}) + f_{\text{grad}}(\mathbf{c}) + f_{\text{ir}}(\mathbf{c})] dV$. The microstructure evolution is controlled by the Cahn-Hilliard (CH) Eq. (3).

Model 2 (GL or AC): The free energy and microstructure are completely described by the order parameter field $\boldsymbol{\eta} = \{\eta_1, \eta_2, \dots, \eta_N\}$. The total free energy is calculated by $F = \int_V [f_{\text{ch}}(\boldsymbol{\eta}) + f_{\text{grad}}(\boldsymbol{\eta}) + f_{\text{ir}}(\boldsymbol{\eta})] dV$. The microstructure evolution is controlled by the time-dependent Ginzburg-Landau (GL) or Allen-Cahn (AC) Eq. (4).

Model 3 (WBM): The free energy and microstructure are described by both concentration field $\mathbf{c} = \{c_1, c_2, \dots, c_M\}$ and order parameter field $\boldsymbol{\eta} = \{\eta_1, \eta_2, \dots, \eta_N\}$. The total free energy is calculated by $F = \int_V [f_{\text{ch}}(\mathbf{c}; \boldsymbol{\eta}) + f_{\text{grad}}(\boldsymbol{\eta}) + f_{\text{ir}}(\mathbf{c}; \boldsymbol{\eta})] dV$. For a two-phase coexistent system with α phase and β phase, the chemical free energies, $f_{\alpha}(\mathbf{c})$ and $f_{\beta}(\mathbf{c})$, for the two respective phases are known, and one order parameter, η , is used to describe different structures of two-phases. The chemical free energy density $f_{\text{ch}}(\mathbf{c}; \eta)$ of two-phase coexisted system is defined as

$$f_{\text{ch}}(\mathbf{c}; \eta) = h(\eta)f_{\alpha}(\mathbf{c}) + [1 - h(\eta)]f_{\beta}(\mathbf{c}) + wg(\eta), \quad (5)$$

where $h(\eta)$ is a shape function related to the volume fraction of α phase at material point \mathbf{x} . $g(\eta)$ is a double-well potential, and w is the height of the double-well potential. Wheeler, Boettinger, and McFadden proposed this so-called “WBM” model for the first time in considering binary alloys.¹¹⁸ The WBM model assumes that α and β phases have the same concentration but different volume fraction at point \mathbf{x} . The microstructure evolution is controlled by the time-dependent Cahn-Hilliard (Eq.(3)) and Ginzburg-Landau Equations (Eq. (4)).

Model 4 (KKS): The free energy and microstructure are described by both concentration field $\mathbf{c} = \{c_1, c_2, \dots, c_M\}$ and order parameter field $\boldsymbol{\eta} = \{\eta_1, \eta_2, \dots, \eta_N\}$. The total free energy is calculated by $F = \int_V [f_{\text{ch}}(\mathbf{c}; \boldsymbol{\eta}) + f_{\text{grad}}(\boldsymbol{\eta}) + f_{\text{ir}}(\mathbf{c}; \boldsymbol{\eta})] dV$. For a two-phase coexistent system, for example, α and β phases, and the chemical free energies, $f_{\alpha}(\mathbf{c})$ and $f_{\beta}(\mathbf{c})$, for the α phase and β phase are known, one order parameter, η , is introduced to describe the microstructure of two-phase system. The chemical free energy density $f_{\text{ch}}(\mathbf{c}; \eta)$ is defined to be the same as Eq. (5), as used in the WBM model, i.e., Model 3. However, Model 4 assumes that the α and β phases at point \mathbf{x} have different concentrations $\mathbf{c}_{\alpha} = \{c_{\alpha,1}, c_{\alpha,2}, \dots, c_{\alpha,M}\}$ and $\mathbf{c}_{\beta} = \{c_{\beta,1}, c_{\beta,2}, \dots, c_{\beta,M}\}$, respectively, yet

with the same chemical potential

$$\begin{aligned} \partial f_{\alpha}(\mathbf{c}_{\alpha}) / \partial c_{\alpha,i} &= \partial f_{\beta}(\mathbf{c}_{\beta}) / \partial c_{\beta,i}, \quad (i = 1, 2, \dots, M) \text{ and} \\ \mathbf{c} &= h(\eta)\mathbf{c}_{\alpha} + (1 - h(\eta))\mathbf{c}_{\beta}. \end{aligned} \quad (6)$$

The model was developed by SG Kim, WT Kim, and Suzuki for a binary alloy system.¹¹⁹ The microstructure evolution is controlled by the time-dependent Cahn-Hilliard (Eq. (3)) and Ginzburg-Landau equations (Eq. (4)).

Model 1 or Model 2 can be used if the material microstructure is completely described by the concentration field or order parameter field. Typical examples can be found in phase separation⁷⁵ and grain growth,⁹¹ respectively. In Model 3 (WBM), every point is assumed to be a mixture of the coexisting phases with the same composition and different volume fractions. Differently, Model 4 (KKS) assumes that the material is a mixture of the coexisting phases, which have the same chemical potential but different concentrations and volume fractions. For Models 2 and 4, through equilibrium and thin interface limit analyses, one can establish the relationships between model parameters and material properties. For Models 1 and 3, since the bulk free energy contributes to the interfacial energy, there is no analytical solution to determine the model parameters. Hence, numerical methods have to be used to determine model parameters. In addition, the advantage of Model 4 is that one can artificially increase the interface thickness while maintaining the thermodynamic and kinetic properties of interfaces (interfacial energy and mobility). As a result, the physical domain of simulation cell and simulation time step can be increased.

By numerically solving the two groups of equations together with appropriate boundary conditions and constraint conditions, including mechanical and chemical equilibriums, one can obtain the spatial and temporal distributions of the PF variables $\mathbf{c} = \{c_1, c_2, \dots, c_M\}$ and $\boldsymbol{\eta} = \{\eta_1, \eta_2, \dots, \eta_N\}$, hence the quantitative descriptions of the microstructure of interest. To simulate and predict material microstructure evolution under irradiation, it is essential to: (a) choose proper PF variables according to the physical phenomena associated with the material process of interest; (b) develop a thermodynamic model by accounting for the main driving forces of microstructure evolution; and (c) correctly describe irradiation defect evolution kinetics, such as one-dimensional motion of SIAs and defect emission, and its impact on thermodynamic and kinetic properties of the system (e.g., phase stability and solute mobility). In the next section, we will review several applications of the PF method in predicting microstructure evolution of irradiated nuclear materials.

Table 1. Applications of PF method in radiation-induced microstructure evolution

Radiation-induced microstructure evolution phenomenon	References
Gas bubble evolution	54–62
Void formation and evolution	63–73
Void and gas bubble lattice formation	62, 74
Void migration	75–77
SIA loop growth and sink strength	78–80
Segregation and precipitation	81–90
Grain growth and recrystallization	91–95

SIMULATIONS OF DIFFERENT PHENOMENA IN RADIATION-INDUCED MICROSTRUCTURE EVOLUTION

Application of the PF approach in irradiated nuclear materials has attracted growing interest because of its unique capability in predicting 3-D microstructure evolutions in a multi-component and multi-phase system. In the past decade, PF models have been used to simulate a number of important microstructure evolution phenomena and their subsequent impact on material thermo-mechanical properties in irradiated materials. Table 1 summarizes the most important applications of the PF method in the irradiated materials domain. In this section, we evaluate in brief the merit, capability, and limitations of the different models.

Gas bubble evolution

With increasing burn up (advance of the fission reactions or time in the reactor), due to the extremely low solubility of fission gas atoms in nuclear fuels, fission gas atoms precipitate and form gas bubbles. The evolution of gas bubbles affects not only fission gas release but also the thermomechanical properties of fuels, including thermal conductivity and volume swelling, which directly impacts nuclear fuel performance and structural integrity. Therefore, understanding and predicting gas bubble evolution kinetics and its subsequent impact on material properties are crucial for scientific design of advanced nuclear fuels, optimizing fuel operation, and reducing uncertainty in operational and safety margins.

Stan et al.⁵⁴ proposed, for the first time, a simple PF model to simulate the evolution of gas bubbles in an irradiated material. In a later work,⁵⁵ a more sophisticated PF model for gas bubble evolution in a polycrystalline was developed. The model considered the coexistence of two phases, i.e., gas bubble and matrix phases. The gas bubbles were assumed to be complex, consisting of gas atoms and vacancies. Gas atom concentration $c_1(\mathbf{x},t) = c_{\text{gas}}(\mathbf{x},t)$ and vacancy concentration $c_2(\mathbf{x},t) = c_{\text{vac}}(\mathbf{x},t)$ were considered as the PF variables. The chemical free energy employed in this study belongs to Model 1, with the free energy being a function of concentrations only. The matrix phase consisted of a polycrystal with dislocations. The GBs and dislocations in the model did not evolve with time and were considered as spatially stationary defects. Their impact on the diffusion of vacancies and gas atoms was through the long-range elastic interaction due to local lattice mismatches. The ratio between gas atoms and vacancies inside the gas bubbles was assumed to vary with gas bubble size in order to satisfy the equation of state of the gas phase. This model enables (1) the study of the effect of elastic interaction among the gas bubbles, diffusive gas atoms and vacancies, dislocations, and GBs on gas bubble nucleation and growth; (2) the examinations of the effect of the thermodynamic and kinetic properties of gas atoms and vacancies on gas bubble evolution kinetics.

Radiation-induced gas resolution, one of the important mechanisms influencing gas bubble evolution kinetics, was integrated into a modified model in the work.⁵⁶ Millett et al.⁵⁸ simulated the evolution of gas bubbles in a polycrystal using the PF method and Model 3 was used to describe the chemical free energy. Their model considered the co-evolution of gas bubbles and grains so captured the dynamic interaction between intra-granular gas bubble and grain growth. Millett et al.^{59, 60} further improved the model to capture the morphology of inter-granular gas bubbles. The model assumed that the equilibrium concentration of gas atoms was 1 inside gas bubbles and 0 in the matrix. Then, a free energy formulation consistent to Model 2 was constructed to describe the inter-granular gas bubbles in polycrystalline materials. The order parameter field of gas concentration satisfied the Cahn-Hilliard equation while the order parameter fields of grain orientations satisfied the Allen-Cahn equation. With the assumed thermodynamic model, an analytical

formula between model parameters (gradient coefficients and height of double wells) and material properties (the interfacial energy and interface thickness) can be obtained by thin interface analysis. Thus, the model allowed one to study the effect of gas bubble wetting angle at GBs on gas bubble evolution and gas release kinetics. The initial bubble density and bubble shape were found to have a strong influence on the rate of bubble percolation and gas release.

The evolution kinetics of intra-granular fission gas bubbles in UO₂ fuels under post-irradiation thermal annealing conditions was studied using the PF method⁶¹ that employed Model 4 (KKS), instead of Model 1 used in ref. 55, in an attempt to employ a physics-based description of chemical free energies. The free energy functional and model parameters were evaluated from atomistic simulations and experiments, while the critical nucleus size of gas bubbles and gas bubble evolution were simulated in a 3-D simulation cell. A linear relationship between logarithmic bubble number density and logarithmic mean bubble diameter was predicted and resulted in good agreement with the experimental data.

Very recently, a more comprehensive PF model of gas bubble evolution in nuclear fuels was developed.⁶² The model took into account the spatial-dependent generation of defects, radiation-induced dissolution, elastic interaction, and one dimensional migration of interstitials and was used to examine the mechanism of Xe gas bubble superlattice formation in irradiated UMo metallic fuels. The simulation showed that the fast one dimensional migration of SIAs along $\langle 110 \rangle$ directions was the dominant mechanism for the fcc Xe gas bubble superlattice formation in bcc UMo fuels.

Gas bubble evolution in irradiated nuclear materials is a complex process that involves mechanisms such as gas bubble homogeneous and heterogeneous nucleation, small gas bubble migration, radiation-induced dissolution, strong anisotropic mobility of defects, elastic interaction, the transition between gas bubbles and voids, and grain growth/recrystallization. Coupling all these mechanisms, as difficult as it is, must be considered in the extension of the current PF models to quantitatively predict critical effects of radiation on microstructures such as porosity evaluation, changes in grain sizes, and gas bubble-induced swelling.

Void nucleation and evolution

There are several works involving PF modeling of void evolution kinetics.^{63–73} Vacancy concentration $c_1(\mathbf{x},t) = c_v(\mathbf{x},t)$ and order parameter $\eta(\mathbf{x},t)$ were used to describe a system containing voids and the matrix. The chemical free energy in the form of Model 3 was employed to simulate void nucleation and growth in both single-crystal⁶³ and polycrystalline metals.⁶⁴ For the polycrystalline case, the static GBs acted as sinks or sources of vacancies in the form of $-S_v^{\text{GB}}(1 - \Phi)(c_v - c_v^{\text{eq}})$, where $\Phi = \sum_{i=1}^p \varphi_i^2$ with φ_i representing a unique grain orientation (see ref. 120 for a description of the polycrystalline model typically used in PF models). Here c_v^{eq} was the thermal equilibrium vacancy concentration in the solid. The parameter S_v^{GB} described the efficiency of either nucleation or annihilation of vacancies and varied with the GB types depending on their structural and/or energetic properties. The value of Φ was equal to 1 inside a grain (eliminating the sink term) and less than 1 at GB and triple junction regions. For oversaturated vacancy concentrations ($c_v > c_v^{\text{eq}}$) near a GB, the GB acted as a vacancy sink. Conversely, a GB with under-saturated vacancy concentrations ($c_v < c_v^{\text{eq}}$) around it acted as a vacancy source. When GBs acted as vacancy sinks, the void denuded zone was obtained from the simulation (shown in Fig. 2).

In a later work, Millett et al.⁶⁶ improved the model by including the evolution of SIAs. The SIA concentration was represented by $c_2(\mathbf{x},t) = c_i(\mathbf{x},t)$. A reaction term between vacancies and SIAs, $R_{iv}(\mathbf{x},t)$

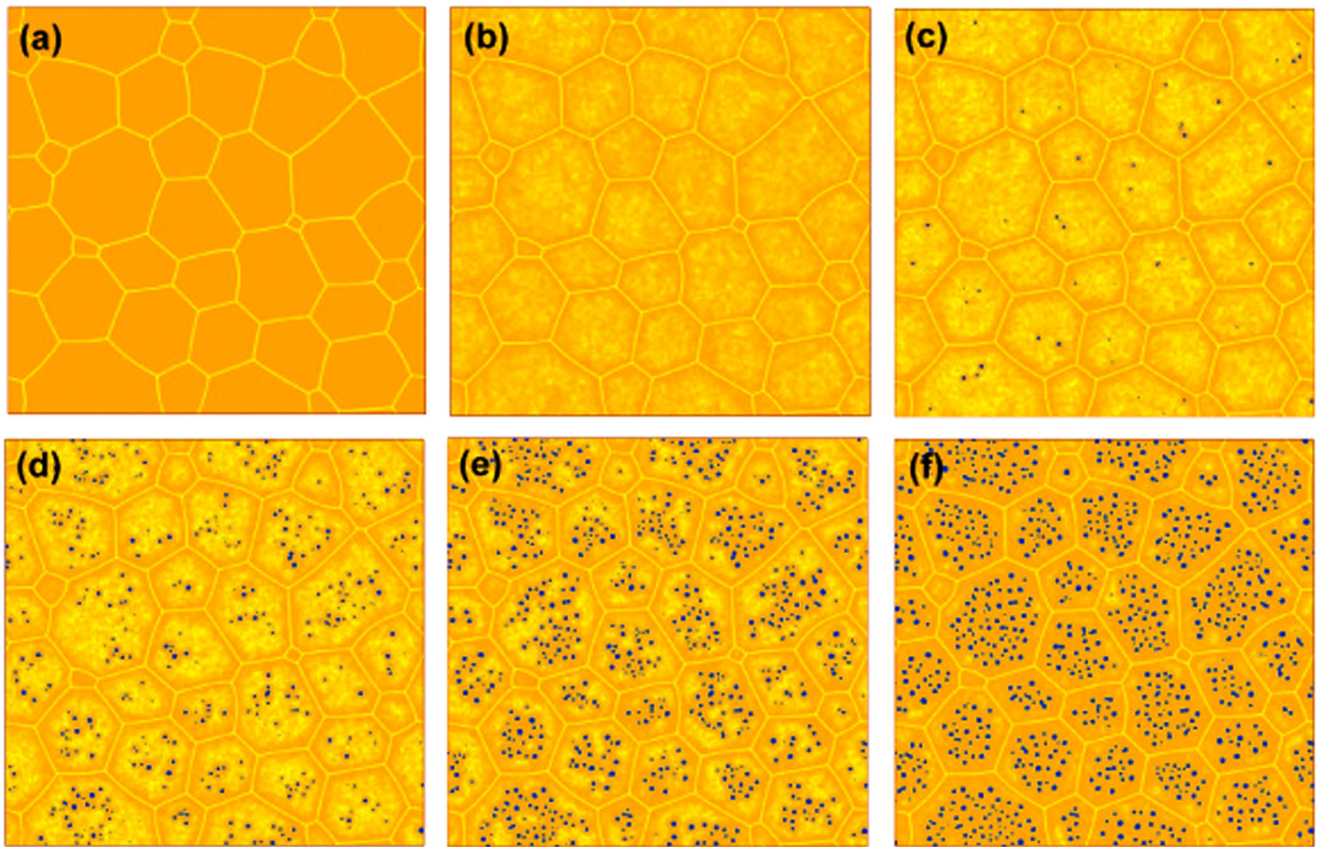


Fig. 2 Formation of void structures and void denuded zones within a polycrystalline microstructure subjected to ongoing vacancy production due to cascades. The figures represent progressive snapshots in time. The initial vacancy concentration was set to the equilibrium value throughout the domain.⁶⁴

$= R_r c_v c_i$, was introduced into the model. R_r was a rate parameter that consisted of both bulk and surface terms: $R_r = R^{\text{bulk}} + \eta^2 R^{\text{surf}}$. This allows a higher rate of recombination at the free surfaces of voids. Different diffusivities of vacancies and SIAs were used in the simulations. Due to the faster diffusion of SIAs compared with vacancies, the SIA depletion zone near a GB was wider than that of the vacancies, leading to the formation of a void peak zone directly adjacent to the void denuded zone, which agreed with experimental observations.

In materials under irradiation, most microstructure such as voids, gas bubbles, and precipitates, forms and evolves via nucleation and growth. Although the PF method can successfully account for growth kinetics, current PF models cannot describe the nucleation process. This is because the PF method assumes that microstructure evolution is driven by the minimization of the system's total free energy while nucleation requires that the system overcomes an energy barrier for such an event. In the FP models of void evolution^{63, 64, 66} the authors stated that the models could describe the nucleation process of voids. However, the statement was incorrect because the void nucleation observed in the simulations occurred with the vacancy concentration larger than the spinodal decomposition concentration. Therefore, the void nucleation was actually via spinodal decomposition. Recently, Semenov and Woo^{67, 68} developed a PF model of void evolution with an accurate thermodynamic model and stochastic fluctuation arising from both correlated point-defect production in collision cascades and random diffusion jumps. Their simulations confirmed that the FP model can correctly describe the thermodynamics of void formation and the resulting equilibrium void size distribution predicted by classical nucleation theory. The model can also correctly describe the evolution of the void assemble as a

process that leads to the minimization of the Cahn-Hilliard type functional. However, in their simulations an extremely small time step (10^{-15} s) was used to ensure numerical stability.⁶⁹

Void and gas bubble lattice formation

Void and gas bubble lattices have been observed in irradiated cladding materials of body-centered cubic (bcc), face-centered cubic (fcc), and hexagonal close-packed (hcp) structures.^{121–124} However, their formation mechanism is not well understood. The PF method was applied to simulate void and gas bubble lattice formation.^{62, 74, 125} The work of Yu and Lu¹²⁵ aimed to examine that the elastic interaction causes the void lattice formation. In the model, vacancy concentration was chosen as the PF variable, i.e., $c_1(\mathbf{x}, t) = c_v(\mathbf{x}, t)$. A chemical free energy of the form of Model 1 was used to describe the matrix and void equilibrium. The long-range interaction energy f_{lr} from elastic interaction was considered, with the inhomogeneous elastic stiffness and lattice mismatch in a solid with distributed voids described as $\lambda_{ijlm} = (1 - c_v)\lambda_{ijlm}^0$, and $\epsilon_{ij}^0 = 2\epsilon_0\delta_{ij}(1 - c_v)c_v$, respectively. Here λ_{ijlm}^0 is the elastic stiffness of the solid. The lattice mismatch ϵ_{ij}^0 indicates that the lattice mismatch tends to zero inside matrix ($c_v = 0$) and voids ($c_v = 1$), and the largest lattice mismatch appears at the void/solid interface. The considered case represented void evolution during a post-irradiation annealing process in a solid. The supersaturated vacancy concentration was set up to be 0.32, which was estimated based on the void volume fraction observed at a later stage of irradiation. The simulations did demonstrate that the elastic interaction led to the formation of void lattice. However, the vacancy concentration used in the simulation was extremely high, which falls in the spinodal decomposition range. The void lattice

formation observed in the simulations was via spinodal decomposition driven by elastic interaction. In irradiated nuclear materials, even at low temperatures, the vacancy concentration remains very low, outside the spinodal decomposition region. In addition, the generation and reaction of defects in irradiated materials plays an important role in void evolution.

Hu and Henager⁷⁴ proposed a PF model integrating first passage kMC method¹²⁶ to simulate the evolution of void ensembles under irradiation. The model used one PF variable, i.e., vacancy concentration, to describe the void microstructure. A chemical free energy of the form of Model 1 was employed in a way similar to ref. 125. The model accounted for the multiple physics including the spatial-dependent generation of vacancies and SIAs, one-dimensional migration of SIAs, 3-D migration of vacancies, reaction among SIAs, vacancies, and voids, as well as cascade-induced heterogeneous nucleation of voids. Small void nuclei associated with the cascade damage were randomly introduced into the simulation cell. The model also considered that SIAs have much larger mobility than vacancies and migrate along close-packed directions or on close-packed atomic planes. The first passage method¹²⁶ was employed to mimic the one-dimensional migration of SIAs while the PF model was used to describe the vacancy diffusion and void evolution. The merit of such a model by coupling PF model and first passage kMC method is to allow for an efficient treatment of the strong anisotropy of diffusivity of defects such as one dimensional migration of interstitials, and huge difference of defect mobility.

The simulation results demonstrated that when the ratio D_{SIA}/D_v was small, the voids had a random distribution where

D_{SIA} and D_v were the diffusivities of SIAs and vacancies, respectively. When D_{SIA}/D_v was larger than 5000, the void lattice started to form. Figure 3 showed the snapshots of void formation when $D_{\text{SIA}}/D_v = 10,000$. It illustrated that (1) voids away from lattice positions shrank because they were not in the shadow of neighboring voids and faced a larger SIA flux; and (2) the shrinking voids caused an increase in local vacancy concentration leading to new void nucleation near void lattice sites. The newly nucleated void, such as the void labeled "C" in the figure, grew and became a void on a site in the perfect void lattice. Larger voids on void lattice sites decreased their growth rate, while smaller voids on lattice sites increased their growth rate. Finally uniform void sizes in the void lattice formed.

The preceding two models have demonstrated that both elastic interaction and one-dimensional SIA movement can result in void lattice formation. It is known that the void-void elastic interaction is strong only when the voids are within a few void diameters of each other. Elastic energy minimization cannot explain how voids organize themselves over relatively long distances, especially during the early stages of irradiation. The one-dimensional SIA migration requires a very high mobility ratio D_{SIA}/D_v for void lattice formation. The simulations demonstrated that the PF models can predict the effect of elastic interaction, one dimensional migration, and radiation conditions on void evolution. However, in order to examine the mechanisms of void lattice formation, the thermal dynamic and kinetic properties such as the elastic field around a void, mobility of defects, and nucleation of voids used in PF models must be first validated against experiments or accurate atomistic simulations.

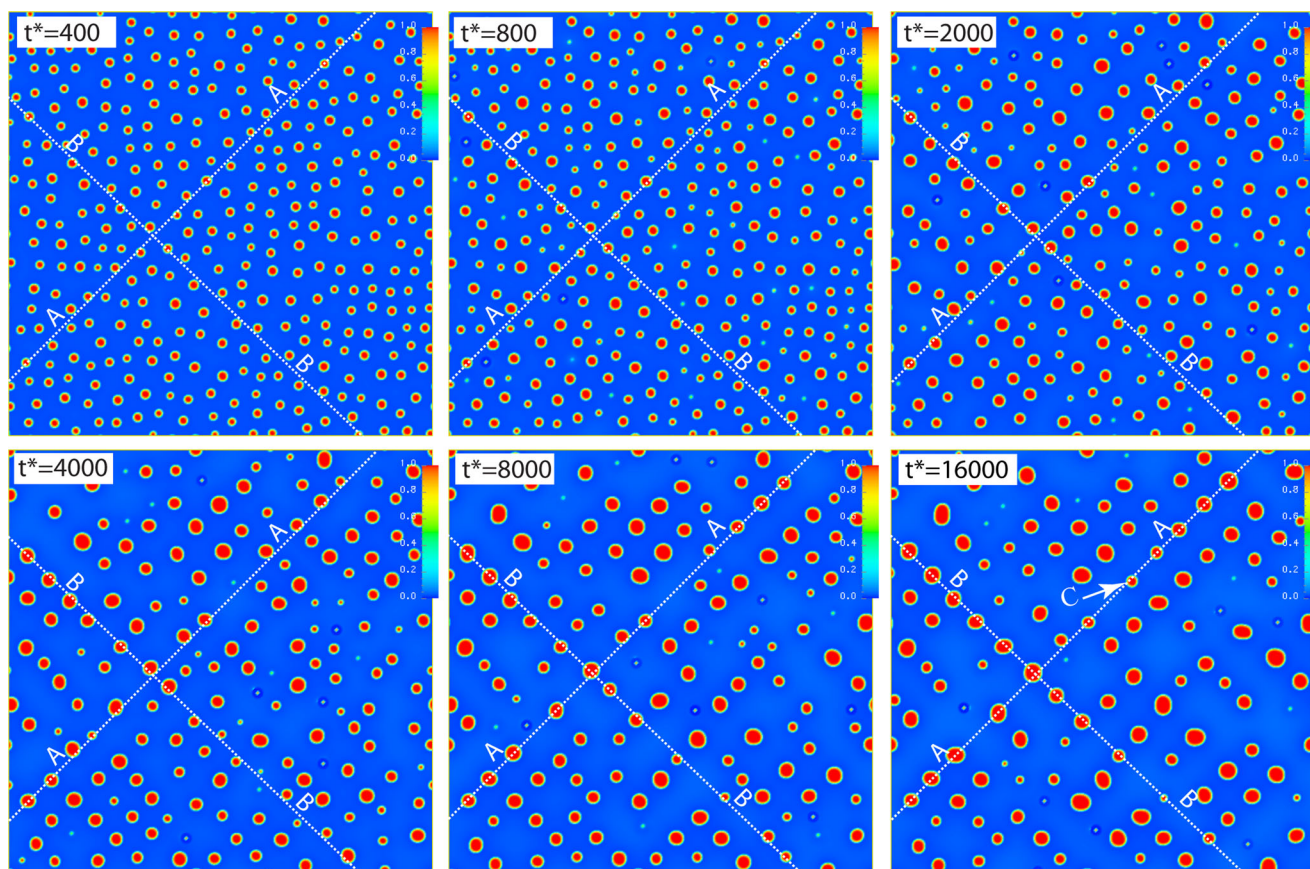


Fig. 3 Temporal evolution of a void ensemble when the generation rates of vacancies and SIAs are $\dot{g}_v^0 = \dot{g}_{\text{SIA}}^0 = 0.00001$ and the diffusivity ratio is $D_{\text{SIA}}/D_v = 10,000$. About 400 void nuclei are randomly introduced into a two-dimensional 512×512 simulation cell during the simulation. t^* is the normalized time (ref. 74)

Void migration

Central holes are often observed in spent nuclear fuels, which are believed to be formed from the migration of voids due to temperature gradients. PF models have been developed to simulate void migration in a temperature gradient.^{75–77} In the models, the concentrations of vacancies and SIAs, $c_1(\mathbf{x}, t) = c_v(\mathbf{x}, t)$ and $c_2(\mathbf{x}, t) = c_i(\mathbf{x}, t)$, were used as variables to describe the distribution of effective vacancies and SIAs, respectively. The chemical free energy density was expressed in the form of Model 1. In addition, the concentration-dependent mobility⁷⁵ and temperature-dependent formation energies of vacancies and SIAs,^{75, 76} respectively, were considered. The simulation demonstrated that the developed model can well describe the Soret effect,⁷⁶ i.e., temperature gradient giving rise to concentration gradients of vacancies and SIAs, respectively. In addition, predicted void migration behaviors of (1) voids migrating up a temperature gradient and (2) the migration velocity varying inversely with void radius were in agreement with theoretical results and experimental observation.

Due to the low thermal conductivity of the voids, the temperature gradient across individual void is increased, which, in turn, accelerates the void migration. Zhang et al.⁷⁷ has directly coupled heat transport to void migration in a temperature gradient. Figure 4 shows the comparison of temperature profile and void position with and without (the reference case) considering the impact of the low thermal conductivity of voids. Instead of incorporating the concept of higher vacancy solubility in the higher temperature zone into the chemical free energy, a temperature gradient was assumed to provide the direct driving force for a vacancy flux in the model, which showed the same feature as refs. 75, 76 that the void migration velocity is inversely proportional to the void radius.

In nuclear fuels, the voids introduced during fabrication or generated during service migrate under a temperature gradient. The developed PF models can predict the effect of thermodynamic and kinetic properties of defects and irradiation conditions on void migration kinetics, and provide important input parameters for larger length scale (e.g., Finite Element Method) simulations of void migration and central hole formation in nuclear fuels.

Self-interstitial atom (SIA) loops or dislocation loops

Self-interstitial atom (SIA) loops, also called dislocation loops, which have a disk-like shape consisting of additional atomic

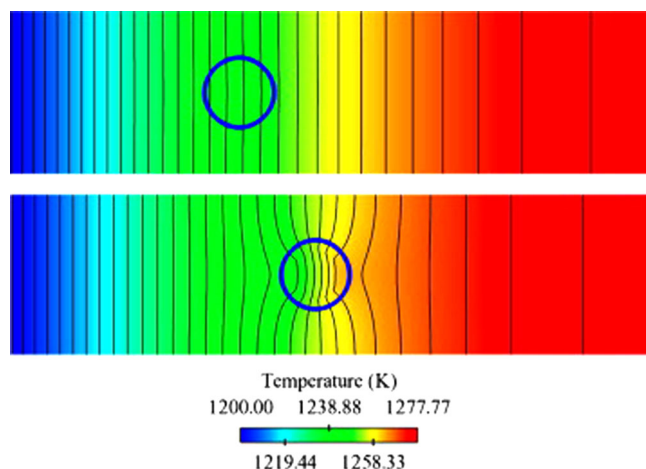


Fig. 4 Comparison of the void position along with the temperature profile after 100 s without (*top*, the reference case) and with (*bottom*) the impact of Xe low thermal conductivity. The contour of voids is demonstrated by $0.1 < c_v < 0.9$ (ref. 77)

layers, are one of the principal evolving defects in irradiated materials. The SIA loop grows by absorbing SIAs and shrinks when vacancies attach on it. Therefore, the formation and evolution of SIA loops affects the accumulation of vacancies and SIAs in the matrix. SIA loops are biased sinks that attract SIAs more strongly than vacancies, which results in the accumulation of vacancies in the matrix and a net vacancy flux entering voids, hence, void grows. They also serve as obstacles of dislocation motion and cause material hardening.

PF models describing the growth kinetics of SIA loops in irradiated materials during aging and under irradiation were developed.^{78, 79} Quantitative investigation of the sink strengths of dislocation loops for point defects through PF modeling was implemented in work.⁸⁰ The PF models considered a phase of SIA loops and a matrix phase with mobile single vacancies and SIAs. In bcc crystal, a SIA loop having a broad {100} plane and Burgers vector of $\mathbf{b} = a \langle 100 \rangle$ is immobile. The loop evolves by absorbing/emitting SIAs. There are three orientation variants of {100} SIA loops. Therefore, to study the {100} SIA loop evolution, five PF variables were used to describe the microstructural features: $c_i(\mathbf{x}, t)$ and $c_v(\mathbf{x}, t)$ for SIA and vacancy concentrations, respectively, and three order parameters $\eta_m(\mathbf{x}, t)$, $m = 1, 2, 3$ for the SIA loops on three different {100} planes. Since all atoms inside the loop are SIAs, the corresponding equilibrium SIA and vacancy concentrations of the loop are $c_i^{\text{eq}}(T) = 1$ and $c_v^{\text{eq}}(T) = 0$, respectively. The order parameter $\eta_m(\mathbf{x}, t)$ equals to 1 within loop m and 0 outside, and varies smoothly from 1 to 0 across the interface between the loop and matrix. The Model 4 of chemical free energy formulation was used to describe the energy landscape of a system with SIA loops. The important feature of SIA loops are their extremely anisotropic interfacial energy. A perfect {100} SIA loop in bcc crystals consists of two atom layers. The broad interface of the SIA loop is coherent to the matrix so the interfacial energy is very small or zero while the interfacial energy along the SIA loop is large, which is determined by the dislocation core energy. The following interfacial energy was used to describe the strong anisotropy of the interfacial energy:

$$f_{\text{grad}}(\eta_m) = \sum_m \frac{\kappa}{2} |\nabla \eta_m|^2 + \sum_m \frac{\kappa_1}{2} |\mathbf{n}_m \times \nabla \eta_m|^2. \quad (7)$$

The first term described the isotropic interfacial energy. The second term described the anisotropic interfacial energy associated with the loop, where \mathbf{n}_m is the unit normal vector of the loop plane. It is zero on the planar interface because \mathbf{n}_m and $\nabla \eta_m$ are parallel vectors. The coefficient κ_1 is related to the loop core energy and much larger than κ in general.

Figure 5 depicted a SIA loop evolution and showed that during the SIA loop growth, the loop thickness remained the same. The model correctly described the morphology of the disk-like SIA loop through the anisotropic interfacial energy. The effect of defect (vacancy/SIA) concentration, generation, recombination, sink strength, and elastic interaction on the growth kinetics of SIA loops can be studied by the model and it was found that the elastic interaction between SIA loops and individual SIAs speeds up the growth of SIA loops.^{78, 79}

Hydride precipitation

Zirconium and its alloys are important structural materials in the nuclear reactors. Their excellent characteristics include good mechanical properties, corrosion resistance, and low neutron absorption cross-section. However, zirconium has a strong affinity for hydrogen, and it gradually picks up hydrogen from the service environment. As a result, the brittle zirconium hydride particles forms in zirconium and its alloys when the hydrogen concentration reaches a certain level. With the growth of hydride particles, a non-uniform internal stress field develops and subsequently microcracks may nucleate and propagate leading to degradation

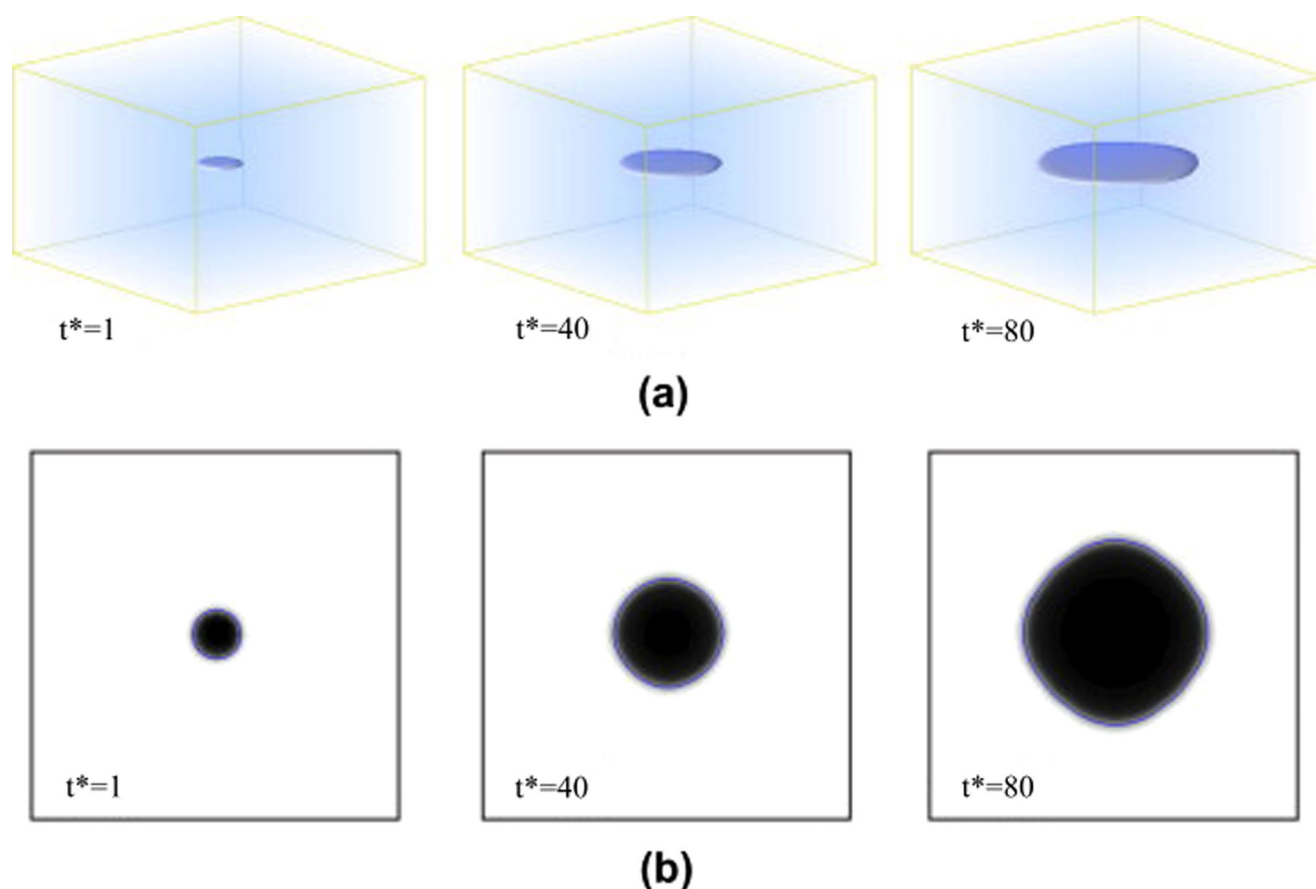


Fig. 5 **a** 3-D snapshots of the morphology evolution of an SIA loop during aging, and **b** the projection on the plane of the SIA loop. t^* is the normalized time (ref. 79)

of the materials' mechanical properties. The PF method was used to simulate the morphological evolution of hydride precipitation and growth in a zirconium bulk material with and without flaws by considering elastic deformation and elastic-plastic deformation, respectively.^{81–87}

In the PF models of hydride precipitation^{81–86} a non-conservative order parameter vector, $\boldsymbol{\eta} = \{\eta_1(\mathbf{x}, t), \eta_2(\mathbf{x}, t), \dots, \eta_N(\mathbf{x}, t)\}$, was used to describe the crystal orientations of hydride precipitates, and a conserved field variable, $c_1(\mathbf{x}, t) = c_H(\mathbf{x}, t)$, was used to describe the concentration of hydrogen in precipitates and matrix. The chemical free energy density was a summation of the forms of Model 1 for the concentration of hydrogen and Model 2 for different orientated hydride precipitates plus their interaction terms. The elastic energy resulting from the lattice mismatch between the precipitates and matrix was taken into account. The precipitation of γ -hydride in zirconium generates three possible equivalent orientation variants with an angle of 120° between each other. The non-zero components of the stress-free transformation strain tensor for the hydride formation are along $[0\ 0\ 0\ 1]$, $[11\text{--}20]$, and $[1\text{--}100]$ directions, respectively. In the simulations, the interfacial energy was assumed to be isotropic. Thermal fluctuations of concentration $c_H(\mathbf{x}, t)$ and order parameter $\eta_k(\mathbf{x}, t)$ were introduced. Figure 6 displayed the nucleation and growth of γ -hydride precipitates. It was found that (1) the morphology of thin needle shaped precipitates is determined by the minimization of the interfacial energy and elastic energy that is a function of shape and orientation of the precipitates; and (2) the long-range elastic interactions among different orientated hydrides strongly affect hydride growth kinetics and microstructures including the size and spatial distributions.

With the model the effect of GBs, external stresses, elastic-plastic deformation, and existing flaws in the zirconium matrix on γ -hydride precipitation in zirconium have been extensively studied. Under applied load, the spatial distribution of hydrides became anisotropic and hydrides aligned perpendicular to the direction of the applied tensile load. For existing hydride platelets, a certain load is required for reorienting them. However, a small applied stress can efficiently affect the nucleation of hydrides, and results in an anisotropic alignment of precipitates. Applied stress not only played an important role in the morphological evolution of hydride precipitates, but also resulted in tensile stresses inside hydride particles, which may initiate cracks at the hydrides. On the other hand, GBs can increase the nucleation density of the hydrides, but their effect was weaker compared with external load. However, the effect of neutron irradiation on hydride precipitation was not considered in the current model. In addition, the simulations were all performed in two dimensions. The anisotropic mobility of hydrogen and defects, anisotropic interfacial energy, and anisotropic deformation field in zirconium and its alloys may strongly affect the hydride precipitation kinetics in three dimensions.

Radiation-induced segregation (RIS) and precipitation

Experiments and simulations show that radiation-enhanced segregation and phase separation is one of important materials property degradation processes. For instance, FeCr alloys undergo radiation-induced phase separation from the solid solution into Cr-rich precipitates in reactor environments. Atom probe experiments showed that the solute concentration inside the Cr-rich cluster was much lower than the thermal equilibrium

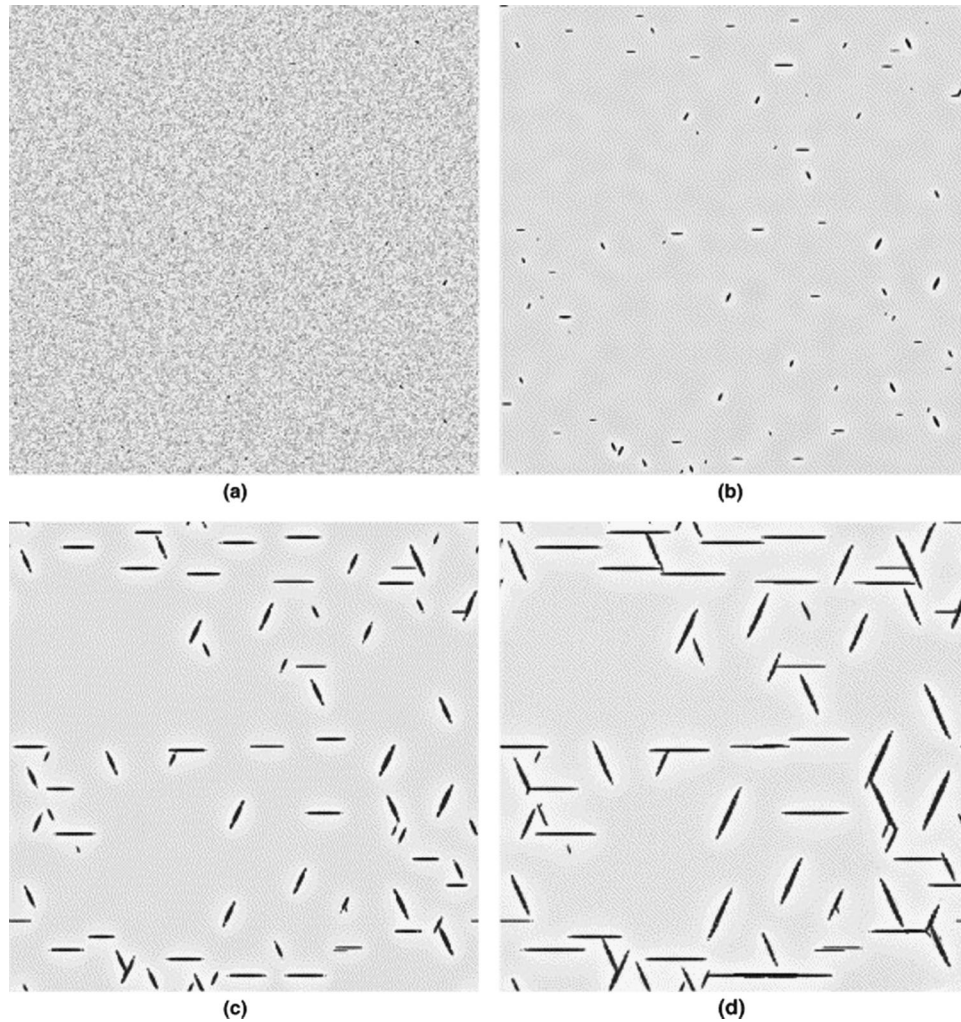


Fig. 6 Simulated precipitation process of γ -hydride from a hexagonal zirconium matrix. The simulation cell was 512×512 uniform grids: **a** $t^* = 1000$; **b** $t^* = 2000$; **c** $t^* = 4000$; **d** $t^* = 6000$, where t^* is the normalized time.⁸²

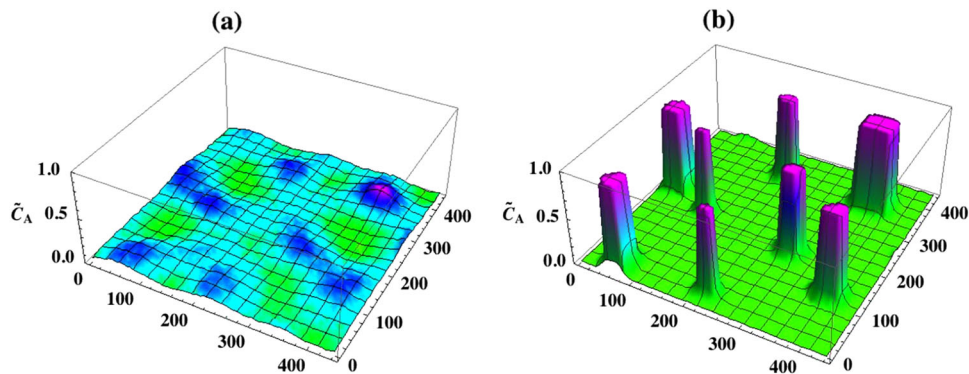


Fig. 7 Radiation-induced homogeneous precipitation in an undersaturated A_6B_{92} alloy with positive heat of mixing (ordering energy of -33.3 MeV). The irradiation displacement rate was 2×10^{-7} dpa s^{-1} , producing Frenkel pairs only; the irradiation dose is **a** 11 dpa and **b** 40 dpa; system contains 64^2 cells, each containing 7×7 lattice sites.⁸⁹

concentration of the precipitates. Li et al.⁸⁸ developed a method by combining the PF method and constrained shrinking dimer dynamics to predict the thermodynamic properties of critical nuclei of precipitates in FeCr alloys. The chemical free energy of FeCr alloys was described by Cr concentration $c_1(\mathbf{x}, t) = c_{Cr}(\mathbf{x}, t)$ and temperature, which has the functional of Model 1. With the

chemical free energy assessed by CALPHAD,¹²⁷ the thermodynamic properties of the critical nuclei of Cr precipitates including the concentration profile, critical size, and nucleation barrier were obtained. The results showed that the maximum concentration in the critical nucleus was much smaller than the thermal equilibrium concentration of $c_{Cr} = 1$. It increased as the temperature increased

and decreased with increasing overall Cr concentration. The results were in good agreement with the observations from atom probe experiments.¹²⁸

Recently, Badillo et al.⁸⁹ proposed a PF model, which integrated the rate theory for studying RIS in a binary model alloy. In the model, the radiation-induced defects were randomly introduced into the simulation cell. Rate theory was used to describe the accumulation and clustering of radiation-induced defects while the PF approach for describing the effect of radiation-induced defects on phase stability and microstructure evolution. The simulations showed that the stochastic fluctuation arising from correlated point-defect production in collision cascades led to the solute segregation and solute rich clusters, which nucleated and grew once the solute concentration inside the clusters was larger than the critical concentration. Figure 7 gave the predicted RIS and precipitates. Like the void nucleation,⁶⁸ the FP model with stochastic fluctuation was able to correctly describe RIS and nucleation of precipitates.

Grain growth and recrystallization

Grain growth and recrystallization are also important features that occur in irradiated nuclear materials and has been investigated with the PF method in nuclear fuels UO₂ and U-7Mo.^{91–95} These modeling expanded the pure grain growth model developed by Chen and Yang¹²⁰ with accounting for the effects of pore/void or gas bubble pinning,^{91, 92} temperature gradient effect,⁹³ initial grain structure,⁹⁴ and dislocation density,⁹⁵ respectively. The non-conserved variables $\{\eta_1(\mathbf{x}, t), \eta_2(\mathbf{x}, t), \dots, \eta_N(\mathbf{x}, t)\}$ were chosen to represent the grain orientations. The temperature gradient was considered as an extra driving force for grain boundary movement and grain growth besides the curvature driving force. It was found that the temperature gradient did not significantly impact the grain growth behavior. However, it did cause local GB motion up the gradient, and a large temperature gradient might affect the growth kinetics of large grains, hence the grain size distribution due to the temperature dependence of the GB mobility.⁹³ To study the pore/gas bubble pinning effect on grain growth, a PF model of grain and pore/gas bubble coevolution has been developed.^{91, 92} The pinning effect was described by the competition between curvature driving grain boundary migration and surface diffusion controlled void migration. The model parameters were linked to the measurable material properties, which allows one to quantitatively investigate the effect of pores on grain growth kinetics.⁹² However, the radiation effect was not taken into account in all the grain growth models.

Very recently, Liang et al.⁹⁵ developed a PF model of radiation-induced recrystallization in U-Mo fuels model. In the model, the rate theory was used to calculate the critical dislocation density, the size and density of critical nuclei of recrystallization grains, which were the input determining the initiation of recrystallization and the nucleation rate of subgrains in the PF modeling. With the assumptions of static recrystallization, grain size independent nucleation rates, and uniform dislocation density, the model was used to study the effect of grain morphology and critical fission density on recrystallization kinetics. Although the presented results were in agreement with experiments the predictive capability of the model might suffer limitation due to the ambiguous treatment of recrystallization location and driving force. For example, why did the recrystallization start at GBs with the assumption of uniform dislocation distribution and how did the grain morphology affect the dislocation distribution? There were some experimental evidences that the recrystallization started at GBs because there was a high dislocation density. It implies that dislocation density is non-uniform in irradiated materials. Therefore, it is crucial to have the spatial evolution of dislocation density in order to model the radiation-induced recrystallization and recrystallization kinetics.

Table 2. Applications of PF method in radiation-induced property degradation

Radiation-induced property degradation	References
Mechanical properties—void and gas bubble swelling	65, 97, 98
Thermal properties—thermal transport and melting	55, 91, 102–106
Magnetic hardening	107, 108

IRRADIATION EFFECTS ON MECHANICAL, THERMAL, AND MAGNETIC PROPERTIES

Besides predicting 3-D microstructure evolutions in a multi-component and multi-phase system, the PF models have been used to evaluate the subsequent impact of microstructure evolution on material properties, mainly focusing in the mechanical, thermal, and magnetic properties. Table 2 summarizes the important applications of the PF method in the irradiated materials properties. In this section, we gave brief review on these applications.

Mechanical properties—void and gas bubble swelling

The PF method was successfully used to predict the effect of microstructure and chemistry on mechanical properties of materials.^{129–132} However, there is no direct application of PF methods to predict the effect of radiation-induced microstructures on mechanical properties. In irradiated materials the most important contribution of the PF method consisted of improving the understanding and prediction of void and gas bubble swelling, which impacts the thermo-mechanical properties of materials.

Void and/or gas bubble swelling is an important phenomenon observed in both nuclear fuels and cladding materials during operation of nuclear reactors. For example, 88% swelling occurs in stainless steel AISI 316 during neutron irradiation at 510 °C in Experimental Breeder Reactor-II (EBR-II).¹²⁶ Such a large volumetric swelling implies a huge microstructure change that results in the degradation of thermo-mechanical properties and affects the structural integrity of material components, as well as the reactor's successful and safe operation. Therefore, swelling is one of key design parameters of reactor components. Extensive experimental^{1–3, 133–135} and computational^{37, 42, 136, 137} studies have been conducted since the void swelling was first observed in 1967 by Cawthorne and Fulton.¹³⁸

A PF model was first developed to simulate this phenomenon in 2011.⁶⁵ In the model, diffusion of both vacancies and SIAs were considered. As such, vacancy and SIA concentrations, $c_v(\mathbf{x}, t)$ and $c_i(\mathbf{x}, t)$, were chosen as the PF variables. A chemical free energy in the form of Model 1 was adopted to describe the void and matrix equilibrium. To study the temperature dependence of void swelling, the effect of temperatures on thermodynamic and kinetic properties, such as chemical free energy, interfacial energy between void and matrix, diffusivity of vacancy and SIAs, and defect generation rates, was taken into account. The results showed a quasi-bell shape distribution of volume swelling in a function of temperature, which is in agreement with experimental results.

Very recently, a 3-D microstructure-dependent swelling model was developed for studying the fission gas swelling kinetics in irradiated nuclear fuels.⁹⁷ The model integrated rate theory (Booth model)¹³⁹ and PF approach. The rate theory was used to describe the intra- and inter-granular gas bubble evolution while the FP model described the effect of heterogeneous microstructures and inhomogeneous thermodynamic and kinetic properties on generation and diffusion of fission products. Figure 8 showed the effect of grain morphology on swelling kinetics obtained from this

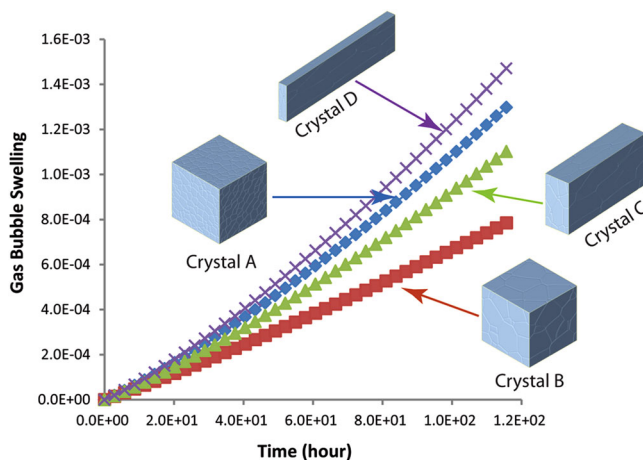


Fig. 8 Effect of grain morphology on gas bubble swelling kinetics under given fission rate $\dot{f} = 2.4 \times 10^{22}$ fission/(m³s) and nucleation factor $f_n = 0.02$. Crystals A and B have the average grain sizes of 1.34 μm , and 4.36 μm , respectively. Crystals B, C, and D have the same average grain volume but different aspect ratios 1:1, 4:1, and 16:1 (ref. 97)

model. It showed that both the decrease of grain size and the increase of grain aspect ratio can speed up swelling. The simulation also demonstrated that the hybrid model of rate theory and FP model can be one powerful simulation tool for the engineering application.

Thermal properties—thermal transport and melting

The primary concern for the present commercial uranium dioxide (UO₂) fuel degradation is its poor thermal conductivity, which can lead to high fuel temperature, fission gas release during irradiation, and reduced safety margins in accident scenarios. The degradation of thermal conductivity due to exposure to high-dose neutron irradiation is a crucial materials issue. Point-defect clustering and growth of radiation-induced voids and fission-gas bubbles can lead to overheating of the central part of fuel elements during use. In addition, grain growth and recrystallization due to overheating and continuing irradiation can also play an important role, as GBs decrease heat transfer.

The above review shows that PF simulations are able to predict 3-D microstructure evolutions including point defect distributions, gas bubble, and void microstructures during irradiation. The output can be used directly to calculate the local thermomechanical properties such as thermal conductivity, and assess the effect of microstructures on effective material properties. For a given microstructure under given temperature (T) or heat flux boundary conditions, the temperature field in a steady state can be obtained by solving the heat conduction equation:

$$\frac{\partial T}{\partial t} = \nabla \cdot K(\mathbf{x}, T) \nabla T = 0, \quad (8)$$

where $K(\mathbf{x}, T)$ is the thermal conductivity, dependent on spatial coordinates and temperature. The effective thermal conductivity along x_1 -direction is calculated by $\bar{K} = \frac{\bar{J}_Q}{\langle \partial T / \partial x_1 \rangle}$, where \bar{J}_Q is the average heat flux and $\langle \partial T / \partial x_1 \rangle$ is the average temperature gradient.

The effect of a polycrystalline material with pores or gas bubbles on thermal conductivity was investigated with the microstructures obtained from PF simulations.^{55, 91, 102–106} The PF models were used to generate the polycrystalline structure with inter- and intra-granular pores/gas bubbles. The GBs, pores, and gas bubbles results in inhomogeneous thermal conductivity so affect the overall material thermal conductivity. Figure 9

displays the calculated effective thermal conductivity of polycrystalline as a function of interface/grain boundary coverage of intergranular gas bubbles and effective thermal conductivity of grains with nano intragranular gas bubbles. The grain boundary coverage was defined as the percentage of grain boundary area covered by the intergranular gas bubbles.

The simulations demonstrated that the complicated microstructure predicted by PF simulations can be directly used to study the effects of microstructures on material thermal conductivity. The microstructures in actual irradiated materials can be very complex, involving second phase precipitates, porosity, gas bubbles, cracks, and their evolution, which subsequently lead to the gradual degradation of properties. Welland et al.^{99–101} applied PF modeling for conducting the coevolution of heat transfer and phase transition to simulate the behavior of nuclear fuel at very high temperatures where center line melting may occur. Through the direct coupling the interaction between the microstructure evolution and inhomogeneous heat transfer can be simulated so the change kinetics of the materials thermal property can be estimated.

Magnetic hardening

The microstructure change under nuclear irradiation affects not only the material's thermo-mechanical properties, but also magnetic properties. For instance, Fe-Cr alloys, which are good candidates for structural materials in fusion and advanced fission reactor components, undergo thermal- and irradiation-induced phase separation in the temperature range of 300 ~ 550 °C. The formation of Cr rich precipitates affect mechanical properties such as strength and ductility as well as magnetic properties. Experiments demonstrated that microcracks generated by the growing precipitates induce demagnetized regions that restrict domain wall movement and result in continuous reduction of remanence during creep.¹⁴⁰ Magnetic hysteresis loops and micro-Vickers hardness measurements in Fe20wt%Cr alloys under isothermal aging or irradiation also showed that magnetic and mechanical hardening are related to Cr precipitate microstructures in FeCr alloys.^{141, 142}

The PF approach incorporating micromagnetic dynamics described by Landau-Lifshitz-Gilbert (LLG) equations¹⁴³ has been developed to study the interaction between magnetic domain walls and microstructural defects.^{107, 108} Simulations showed that the presence of nonmagnetic particles can cause magnetic hardening. The impact of nonmagnetic particle sizes on magnetic domain switching and the coercive field were shown in Fig. 10. The developed model enables one to investigate the interaction mechanisms between nonmagnetic particles and magnetic domain walls, improve the understanding of signal physics of non-destructive magnetic measurements, and provide the guidance for the development of advanced monitoring techniques for non-destructively detecting material degradations under thermal and irradiation environments.

CONCLUSIONS

The PF method is based on the fundamental thermodynamic laws, the kinetics of defects in the system under examination, and the understanding of the mechanisms behind the material processes. While acknowledging the successes of the PF method in predicting microstructure evolution in solidification and solid state phase transitions, the focus of this review is on examining the role of the PF method in predicting microstructure evolution in irradiated nuclear materials, and the impact on their properties.

The landscape of irradiation effects on reactor materials is complex: from dimensional changes associated with void and/or gas bubble swelling, to changes in local chemistry and microstructure, all the way to changes in mechanical, chemical,

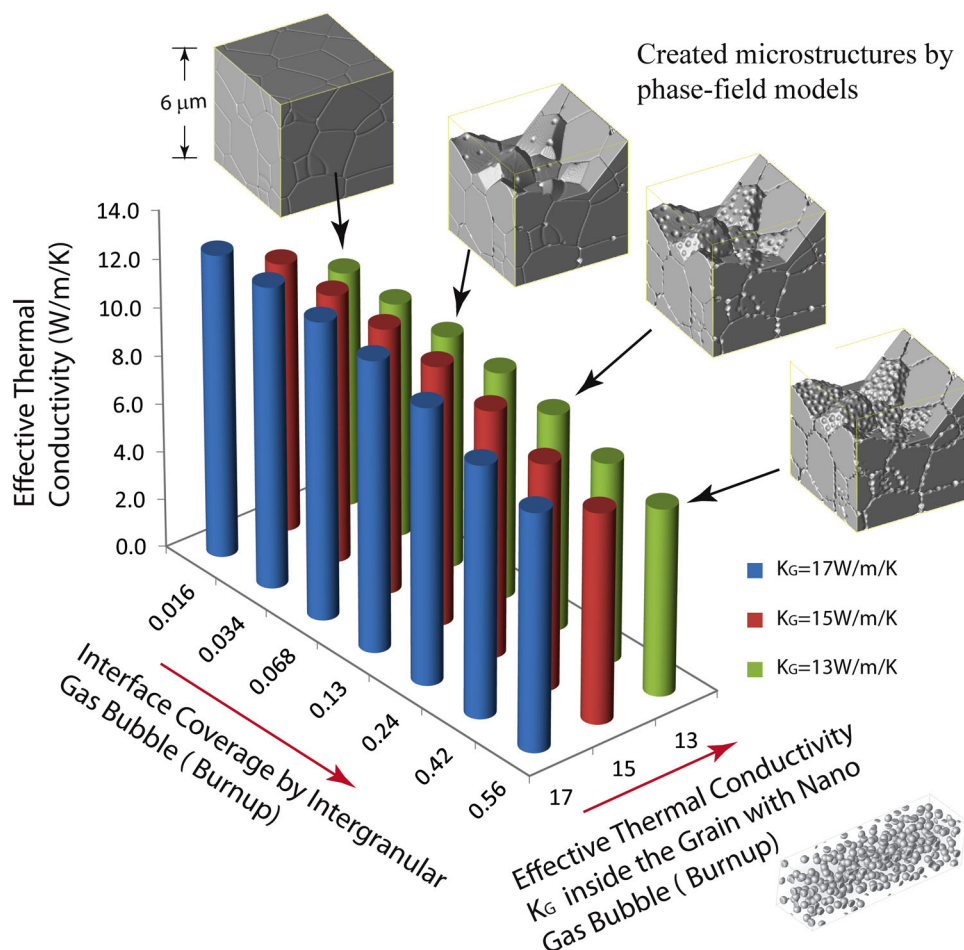


Fig. 9 Calculated effective thermal conductivity of U-10wt%Mo polycrystalline as a function of interface coverage of intergranular gas bubbles and effective thermal conductivity of grains with nano-scale intragranular gas bubbles¹⁰⁶

and thermal properties. In the context of multiple time and length scale computational methods such as DFT, MD, kMC, cluster dynamics, rate theory, and FEM, a legitimate question is “What does the PF method provide to the understanding of radiation effects, that other methods cannot?” We conclude that the PF method plays the critical role of improving the fundamental understanding, representation, and prediction of the 3-D evolution of the radiation-induced, heterogeneous microstructural features and the impact on material properties, as discussed in the last section. The 3-D spatial distribution of heterogeneous microstructural changes provided by the PF method is crucial to the development of advanced radiation tolerant materials, which can significantly improve the life extension of current reactor fleet and impact the design of advanced reactors.

Microstructure evolution in irradiated materials is a non-equilibrium process that requires the system to overcome energy barriers. So “How can a free energy minimization method describe irradiation effects?” Part of the answer resides in the assumption that the laws of thermodynamics are universal and—when applied correctly—describe well both equilibrium and non-equilibrium processes. PF models are based on the fundamental understanding of the mechanisms behind the materials processes. As shown in the last two review sections, both thermodynamic and kinetic properties of species, defects, and different phases are included in the PF method for predicting microstructure and property evolution. For example, the PF methods with an accurate thermodynamic model and stochastic fluctuation arising from both correlated point-defect production in collision cascades can

correctly predict the equilibrium cluster distribution as shown in the subsection of void nucleation and evolution and the subsection of RIS and precipitation, hence the nucleation process, and correctly describe the microstructure evolution. The second part of the answer relies on observing the limitations (applicability limits) of various models. For example, PF methods do not attempt to simulate the nucleation of second phases such as voids or gas bubbles because extremely small length and time scales are required, and rely on other theoretical and computational approaches to generate that information. With the nucleation rate and critical nucleus information as input from classical nucleation theory and lower level atomistic simulations, the PF method evolves the phases, which is well equipped of doing.

A major objective of the review was to answer the question “Is the PF method qualitative or quantitative?” We conclude that, in the area of radiation effects on nuclear materials, the existing PF models are overwhelmingly qualitative because mesoscale microstructure evolution is a very complicated process, especially in irradiated materials. Many factors might affect the microstructure evolution kinetics including initial microstructures, second phase nucleation kinetics, applied fields, and interaction among different physical processes. In addition, most simulations were carried out with extremely high defect concentrations and in 2-D due to the limitation of current computer capability while the phenomenon is in 3-D. However, a qualitative modeling capability is not a bad thing. The conclusion is based on two observations: First, simulated microstructures are not copies (replicas) of real (experimentally observed) microstructures. As a consequence,

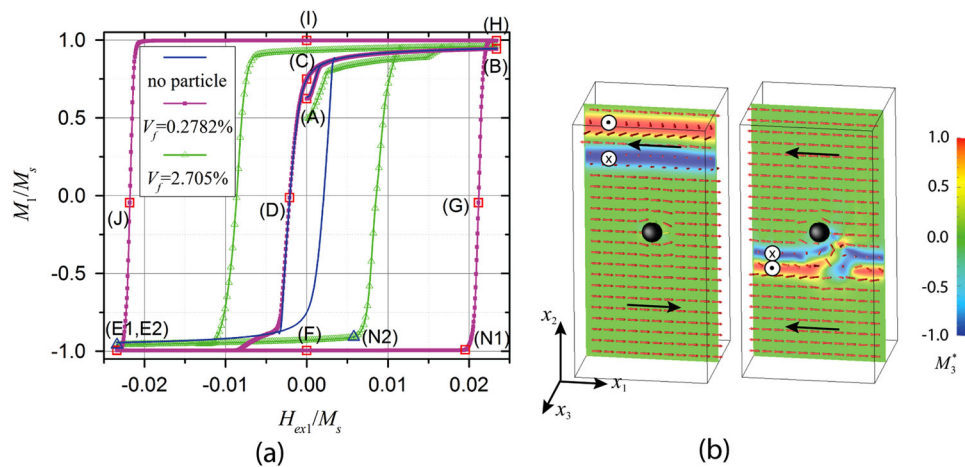


Fig. 10 **a** Magnetic hysteresis loops for the cases of $V_f = 0.0$ (no particle), $V_f = 0.2782\%$, and $V_f = 2.705\%$, respectively. V_f is the volume fraction of the nonmagnetic sphere with respect to the simulation cell. For the case of $V_f = 0.2782\%$, the loop follows the sequence of (ABCDE₁FN₁GHIJ). **b** Magnetic domain morphology snapshots of the central x_1x_2 plane, where the *black sphere* is a nonmagnetic particle. The *outside box* is the 3-D simulation cell, *black arrows* are the magnified magnetization vectors shown in the corresponding domains, and the color illustrates the magnitude of the magnetization component M_3^* as depicted by the color bar (e.g., *blue* is into the page indicated as \otimes , and *red* is out of the page indicated as \odot)¹⁰⁷

the qualitative aspect of the PF predictions is the most important one. For example, the successful predictions of void and gas bubble swelling reviewed in the first part of irradiation effects on materials properties employ representations in terms of average grain sizes and average grain aspect ratio. What makes the PF method more valuable than other similar method is the prediction of 2-D or 3-D spatial distribution of voids and bubbles that makes it possible to compare, even qualitatively, with experimental irradiated microstructures, and to improve the understanding of the dominate mechanisms and physics behind the complicated material process. Second, computer simulation results are more transferable to real materials when expressed in terms of differences or derivatives (rates), rather than absolute values. As an example, the FP model with stochastic fluctuation was able to correctly describe RIS and nucleation of precipitates. The correlation between the rate of producing defect and the dose is the useful information—even though qualitative (approximate)—for estimating damage in specific alloys. However, the long-term goal for the development of mesoscale PF models is to improve their predictive capability by integrating precise and accurate thermodynamic and kinetic property models and the key mechanisms behind the material process.

To another important question, “Is the PF method computationally efficient?” the review led to an unambiguous, positive answer. In fact, the simplicity of the implementation, robustness, and the elimination of singularities at the phase boundaries made PF a method of choice. As with any computational method, going beyond the limits of applicability requires coupling with approaches that are valid at adjacent length or time scales. For example, the spatial and temporal correlations in defect production and the effect of long-range interactions are extremely difficult to account for in most methods, especially in materials with strongly heterogeneous microstructures. Capturing the complicated microstructures and heterogeneous thermodynamic and kinetic properties is computationally efficient in the PF method. However, rate theory and kMC are good at handling clustering process of radiation defects. Therefore, coupling PF with cluster dynamic methods, such as rate theory, OkMC, and first-passage kMC can provide a path to more precise, accurate, and computationally efficient simulations of radiation damage in materials. Regarding numerical efficiency in solving the PF

equations, adaptive mesh could be used to reduce the computational cost for simple microstructures or low fraction of moving boundaries. In irradiated materials, the microstructures such as voids, second phase precipitates, and gas bubbles usually have very high volume fraction of interface. These boundaries evolve during nucleation, growth and shrinkage of second phases. Furthermore, most material process involves diffusion of species. The smallest grid size will determine the time step. Therefore, adaptive mesh is not a promising approach to increase the computational efficiency. However, PF modeling of 3-D microstructure evolution requires highly scalable method like the one reported in ref. 144 where millions of computer cores were used to solve the PF equations.

ACKNOWLEDGEMENTS

This work was supported by the US Department of Energy’s Nuclear Energy Advanced Modeling and Simulation (NEAMS) Program in Pacific Northwest National Laboratory (PNNL), which is operated by Battelle Memorial Institute for the US Department of Energy under Contract No. DE-AC05-76RL01830. We greatly appreciated Prof. Long-Qing Chen’s encouragement and suggestion for completing this review work.

AUTHOR CONTRIBUTIONS

All authors contributed equally to this work. S.H. and Y.L. had primary reviewing and writing responsibility. M.S. formulated the key questions and did critical revision of the conclusions. X.S. led the NEAMS project at PNNL, initiated the review, and organized the partnership.

COMPETING INTERESTS

The authors declare no conflict of interest.

REFERENCES

1. Little, E. A. Void-swelling in irons and ferritic steels.1. Mechanisms of swelling suppression. *J. Nucl. Mater.* **87**, 11–24 (1979).
2. Little, E. A. & Stow, D. A. Void-swelling in irons and ferritic steels. 2. Experimental survey of materials irradiated in a fast-reactor. *J. Nucl. Mater.* **87**, 25–39 (1979).
3. Marwick, A. D. Segregation in irradiated alloys - inverse Kirkendall effect and effect of constitution on void swelling. *J. Phys. F-Met. Phys.* **8**, 1849–1861 (1978).

4. Mansur, L. K. Void swelling in metals and alloys under irradiation - assessment of theory. *Nucl. Technol.* **40**, 5–34 (1978).
5. Singh, B. N., Eldrup, M., Zinkle, S. J. & Golubov, S. I. On grain-size-dependent void swelling in pure copper irradiated with fission neutrons. *Philos. Mag. A* **82**, 1137–1158 (2002).
6. Terentyev, D., Haghighat, S. M. H. & Schaublin, R. Strengthening due to Cr-rich precipitates in Fe-Cr alloys: effect of temperature and precipitate composition. *J. Appl. Phys.* **107**, 061806 (2010).
7. Garner, F. A., Toloczko, M. B. & Sencer, B. H. Comparison of swelling and irradiation creep behavior of fcc-austenitic and bcc-ferritic/martensitic alloys at high neutron exposure. *J. Nucl. Mater.* **276**, 123–142 (2000).
8. Scott, P. A review of irradiation assisted stress-corrosion cracking. *J. Nucl. Mater.* **211**, 101–122 (1994).
9. Was, G. S. et al. Corrosion and stress corrosion cracking in supercritical water. *J. Nucl. Mater.* **371**, 176–201 (2007).
10. Tan, L., Ren, X., Sridharan, K. & Allen, T. R. Corrosion behavior of Ni-base alloys for advanced high temperature water-cooled nuclear plants. *Corros. Sci.* **50**, 3056–3062 (2008).
11. Okada, O., Nakata, K. & Kasahara, S. Effects of thermal sensitization on radiation-induced segregation in type 304 stainless steel irradiated with He-ions. *J. Nucl. Mater.* **265**, 232–239 (1999).
12. Wilkes, P. Phase-stability under irradiation—review of theory and experiment. *J. Nucl. Mater.* **83**, 166–175 (1979).
13. Maydet, S. I. & Russell, K. C. Precipitate stability under irradiation—point-defect effects. *J. Nucl. Mater.* **64**, 101–114 (1977).
14. Turnbull, J. A. & Cornell, R. M. Observations demonstrating re-solution of gas from bubbles and sintering pores during irradiation of uo2 at a high temperature. *J. Nucl. Mater.* **37**, 355–357 (1970).
15. Olander, D. R. & Wongsawaeng, D. Re-solution of fission gas—a review: Part I. Intragranular bubbles. *J. Nucl. Mater.* **354**, 94–109 (2006).
16. Johnson, P. B. & Mazey, D. J. Gas-bubble superlattice formation in bcc metals. *J. Nucl. Mater.* **218**, 273–288 (1995).
17. Trinkaus, H. & Singh, B. N. Helium accumulation in metals during irradiation—where do we stand? *J. Nucl. Mater.* **323**, 229–242 (2003).
18. Zacharie, I. et al. Thermal treatment of uranium oxide irradiated in pressurized water reactor: swelling and release of fission gases. *J. Nucl. Mater.* **255**, 85–91 (1998).
19. Dvoriashin, A. M. et al. Mechanical properties and microstructure of three Russian ferritic/martensitic steels irradiated in BN-350 reactor to 50 dpa at 490 degrees C. *J. Nucl. Mater.* **367**, 92–96 (2007).
20. Braski, D. N., Schroeder, H. & Ullmaier, H. Effect of tensile-stress on the growth of helium bubbles in an austenitic stainless-steel. *J. Nucl. Mater.* **83**, 265–277 (1979).
21. Zacharie, I. et al. Microstructural analysis and modelling of intergranular swelling of an irradiated UO2 fuel treated at high temperature. *J. Nucl. Mater.* **255**, 92–104 (1998).
22. Trinkaus, H., Singh, B. N. & Foreman, A. J. E. Impact of glissile interstitial loop production in cascades on defect accumulation in the transient. *J. Nucl. Mater.* **206**, 200–211 (1993).
23. Bacon, D. J., Gao, F. & Osetsky, Y. N. The primary damage state in fcc, bcc and hcp metals as seen in molecular dynamics simulations. *J. Nucl. Mater.* **276**, 1–12 (2000).
24. Osetsky, Y. N., Bacon, D. J., Serra, A., Singh, B. N. & Golubov, S. I. Stability and mobility of defect clusters and dislocation loops in metals. *J. Nucl. Mater.* **276**, 65–77 (2000).
25. Becquart, C. S. et al. Effect of displacement cascade structure and defect mobility on the growth of point defect clusters under irradiation. *J. Nucl. Mater.* **351**, 39–46 (2006).
26. Vortler, K., Bjorkas, C., Terentyev, D., Malerba, L. & Nordlund, K. The effect of Cr concentration on radiation damage in Fe-Cr alloys. *J. Nucl. Mater.* **382**, 24–30 (2008).
27. Domain, C. & Legris, A. Ab initio atomic-scale determination of point-defect structure in hcp zirconium. *Philos. Mag. A* **85**, 569–575 (2005).
28. Klaver, T. P. C., Olsson, P. & Finnis, M. W. Interstitials in FeCr alloys studied by density functional theory. *Phys. Rev. B* **76**, 214110 (2007).
29. Klaver, T. P. C., Hepburn, D. J. & Ackland, G. J. Defect and solute properties in dilute Fe-Cr-Ni austenitic alloys from first principles. *Phys. Rev. B* **85**, 174111 (2012).
30. Dudarev, S. L. Density functional theory models for radiation damage. *Ann. Rev. Mater. Res.* **43**, 35–61 (2013).
31. Soneda, N., Ishino, S., Takahashi, A. & Dohi, K. Modeling the microstructural evolution in bcc-Fe during irradiation using kinetic Monte Carlo computer simulation. *J. Nucl. Mater.* **323**, 169–180 (2003).
32. Caturla, M. J., Soneda, N., de la Rubia, T. D. & Fluss, M. Kinetic Monte Carlo simulations applied to irradiated materials: the effect of cascade damage in defect nucleation and growth. *J. Nucl. Mater.* **351**, 78–87 (2006).
33. Heinisch, H. L. Computer-simulation of high-energy displacement cascades. *Radiat. Eff. Defects Solids* **113**, 53–73 (1990).
34. Torre, J. D., Fu, C. C., Willaime, F., Barbu, A. & Bocquet, J. L. Resistivity recovery simulations of electron-irradiated iron: Kinetic Monte Carlo versus cluster dynamics. *J. Nucl. Mater.* **352**, 42–49 (2006).
35. Domain, C., Becquart, C. S. & Malerba, L. Simulation of radiation damage in Fe alloys: an object kinetic Monte Carlo approach. *J. Nucl. Mater.* **335**, 121–145 (2004).
36. Woo, C. H. & Singh, B. N. Production bias due to clustering of point-defects in irradiation-induced cascades. *Philos. Mag. A* **65**, 889–912 (1992).
37. Surh, M. P., Sturgeon, J. B. & Wolfer, W. G. Master equation and Fokker-Planck methods for void nucleation and growth in irradiation swelling. *J. Nucl. Mater.* **325**, 44–52 (2004).
38. Xu, D. H., Wirth, B. D., Li, M. M. & Kirk, M. A. Defect microstructural evolution in ion irradiated metallic nanofibers: Kinetic Monte Carlo simulation versus cluster dynamics modeling and in situ transmission electron microscopy experiments. *Appl. Phys. Lett.* **101**, 101905 (2012).
39. Xu, D. H., Wirth, B. D., Li, M. M. & Kirk, M. A. Combining in situ transmission electron microscopy irradiation experiments with cluster dynamics modeling to study nanoscale defect agglomeration in structural metals. *Acta Mater.* **60**, 4286–4302 (2012).
40. Surh, M. P., Sturgeon, J. B. & Wolfer, W. G. Radiation swelling behavior and its dependence on temperature, dose rate and dislocation structure evolution. *J. Nucl. Mater.* **341**, 235–236 (2005). vol 336, pg 217, 2004.
41. Ortiz, C. J., Caturla, M. J., Fu, C. C. & Willaime, F. He diffusion in irradiated alpha-Fe: an ab-initio-based rate theory model. *Phys. Rev. B* **75**, 100102 (2007).
42. Brailsford, A. D. & Bullough, R. The rate theory of swelling due to void growth in irradiated metals. *J. Nucl. Mater.* **44**, 121–135 (1972).
43. Singh, B. N. & Zinkle, S. J. Defect accumulation in pure fcc metals in the transient regime—a review. *J. Nucl. Mater.* **206**, 212–229 (1993).
44. Fu, C. C., Dalla Torre, J., Willaime, F., Bocquet, J. L. & Barbu, A. Multiscale modelling of defect kinetics in irradiated iron. *Nat. Mater.* **4**, 68–74 (2005).
45. Stan, M. Discovery and design of nuclear fuels. *Mater. Today* **12**, 20–28 (2009).
46. Chen, L. Q. Phase-field models for microstructure evolution. *Ann. Rev. Mater. Res.* **32**, 113–140 (2002).
47. Granasy, L., Pusztai, T. & Warren, J. A. Modelling polycrystalline solidification using phase field theory. *J. Phys. -Condes. Matter.* **16**, R1205–R1235 (2004).
48. Moelans, N., Blanpain, B. & Wollants, P. An introduction to phase-field modeling of microstructure evolution. *Calphad* **32**, 268–294 (2008).
49. Steinbach, I. Phase-field models in materials science. *Modell. Simul. Mater. Sci. Eng.* **17**, 073001 (2009).
50. Steinbach, I. Phase-field model for microstructure evolution at the mesoscopic scale. *Ann. Rev. Mater. Res.* **43**, 89–107 (2013).
51. Wang, Y. Z. & Li, J. Phase field modeling of defects and deformation. *Acta Mater.* **58**, 1212–1235 (2010).
52. Mamivand, M., Zaeem, M. A. & El Kadiri, H. A review on phase field modeling of martensitic phase transformation. *Comput. Mater. Sci.* **77**, 304–311 (2013).
53. Karma, A. & Rappel, W. J. Quantitative phase-field modeling of dendritic growth in two and three dimensions. *Phys. Rev. E* **57**, 4323–4349 (1998).
54. Stan, M. et al. Models and simulations of nuclear fuel materials properties. *J. Alloy. Compd.* **444**, 415–423 (2007).
55. Hu, S. et al. Phase-field modeling of gas bubbles and thermal conductivity evolution in nuclear fuels. *J. Nucl. Mater.* **392**, 292–300 (2009).
56. Hu, S. et al. Application of the phase-field method in predicting gas bubble microstructure evolution in nuclear fuels. *Int. J. Mater. Res.* **101**, 515–522 (2010).
57. Millett, P. C. & Tonks, M. Phase-field simulations of gas density within bubbles in metals under irradiation. *Comput. Mater. Sci.* **50**, 2044–2050 (2011).
58. Millett, P. C., El-Azab, A. & Wolf, D. Phase-field simulation of irradiated metals Part II: gas bubble kinetics. *Comput. Mater. Sci.* **50**, 960–970 (2011).
59. Millett, P. C., Tonks, M. & Biner, S. B. Mesoscale modeling of intergranular bubble percolation in nuclear fuels. *J. Appl. Phys.* **111**, 083511 (2012).
60. Millett, P. C. et al. Phase-field simulation of intergranular bubble growth and percolation in bicrystals. *J. Nucl. Mater.* **425**, 130–135 (2012).
61. Li, Y., Hu, S., Montgomery, R., Gao, F. & Sun, X. Phase-field simulations of intragranular fission gas bubble evolution in UO2 under post-irradiation thermal annealing. *Nucl. Instrum. Methods Phys. Res. B* **303**, 62–67 (2013).
62. Hu, S. et al. Formation mechanism of gas bubble superlattice in UMo metal fuels: phase-field modeling investigation. *J. Nucl. Mater.* **479**, 202–215 (2016).
63. Rokkam, S., El-Azab, A., Millett, P. & Wolf, D. Phase field modeling of void nucleation and growth in irradiated metals. *Modell. Simul. Mater. Sci. Eng.* **17**, 064002 (2009).
64. Millett, P. C., Rokkam, S., El-Azab, A., Tonks, M. & Wolf, D. Void nucleation and growth in irradiated polycrystalline metals: a phase-field model. *Modell. Simul. Mater. Sci. Eng.* **17**, 064003 (2009).

65. Li, Y. et al. Phase-field modeling of void evolution and swelling in materials under irradiation. *Sci. China-Phys. Mech. Astron.* **54**, 856–865 (2011).
66. Millett, P. C., El-Azab, A., Rokkam, S., Tonks, M. & Wolf, D. Phase-field simulation of irradiated metals Part I: Void kinetics. *Comput. Mater. Sci.* **50**, 949–959 (2011).
67. Semenov, A. A. & Woo, C. H. Interfacial energy in phase-field emulation of void nucleation and growth. *J. Nucl. Mater.* **411**, 144–149 (2011).
68. Semenov, A. A. & Woo, C. H. Phase-field modeling of void formation and growth under irradiation. *Acta Mater.* **60**, 6112–6119 (2012).
69. Xiao, Z. H., Semenov, A. A., Woo, C. H. & Shi, S. Q. Single void dynamics in phase field modeling. *J. Nucl. Mater.* **439**, 25–32 (2013).
70. Wang, N., Rokkam, S., Hochrainer, T., Pernice, M. & El-Azab, A. Asymptotic and uncertainty analyses of a phase field model for void formation under irradiation. *Comput. Mater. Sci.* **89**, 165–175 (2014).
71. El-Azab, A., Ahmed, K., Rokkam, S. & Hochrainer, T. Diffuse interface modeling of void growth in irradiated materials. Mathematical, thermodynamic and atomistic perspectives. *Curr. Opin. Solid State Mater. Sci.* **18**, 90–98 (2014).
72. Semenov, A. A. & Woo, C. H. Modeling void development in irradiated metals in the phase-field framework. *J. Nucl. Mater.* **454**, 60–68 (2014).
73. Hochrainer, T. & El-Azab, A. A sharp interface model for void growth in irradiated materials. *Philos. Mag.* **95**, 948–972 (2015).
74. Hu, S. & Henager, C. H. Jr Phase-field modeling of void lattice formation under irradiation. *J. Nucl. Mater.* **394**, 155–159 (2009).
75. Hu, S. Y. & Henager, C. H. Jr Phase-field simulation of void migration in a temperature gradient. *Acta Mater.* **58**, 3230–3237 (2010).
76. Li, Y. et al. Phase-field modeling of void migration and growth kinetics in materials under irradiation and temperature field. *J. Nucl. Mater.* **407**, 119–125 (2010).
77. Zhang, L. Z. et al. Phase-field modeling of temperature gradient driven pore migration coupling with thermal conduction. *Comput. Mater. Sci.* **56**, 161–165 (2012).
78. Hu, S. et al. Evolution kinetics of interstitial loops in irradiated materials: a phase-field model. *Modell. Simul. Mater. Sci. Eng.* **20**, 015011 (2012).
79. Li, Y. et al. Computer simulations of interstitial loop growth kinetics in irradiated bcc Fe. *J. Nucl. Mater.* **427**, 259–267 (2012).
80. Rouchette, H., Thuinet, L., Legris, A., Ambard, A. & Domain, C. Quantitative phase field model for dislocation sink strength calculations. *Comput. Mater. Sci.* **88**, 50–60 (2014).
81. Ma, X. Q., Shi, S. Q., Woo, C. H. & Chen, L. Q. Phase-field simulation of hydride precipitation in bi-crystalline zirconium. *Scr. Mater.* **47**, 237–241 (2002).
82. Ma, X. Q., Shi, S. Q., Woo, C. H. & Chen, L. Q. Effect of applied load on nucleation and growth of gamma-hydrides in zirconium. *Comput. Mater. Sci.* **23**, 283–290 (2002).
83. Ma, X. Q., Shi, S. Q., Woo, C. H. & Chen, L. Q. Simulation of gamma-hydride precipitation in bi-crystalline zirconium under uniformly applied load. *Mater. Sci. Eng. A-Struct. Mater. Prop. Microstruct. Process.* **334**, 6–10 (2002).
84. Ma, X. Q., Shi, S. Q., Woo, C. H. & Chen, L. Q. The phase field model for hydrogen diffusion and gamma-hydride precipitation in zirconium under non-uniformly applied stress. *Mech. Mater.* **38**, 3–10 (2006).
85. Guo, X. H., Shi, S. Q., Zhang, Q. M. & Ma, X. Q. An elastoplastic phase-field model for the evolution of hydride precipitation in zirconium. Part I: smooth specimen. *J. Nucl. Mater.* **378**, 110–119 (2008).
86. Guo, X. H., Shi, S. Q., Zhang, Q. M. & Ma, X. Q. An elastoplastic phase-field model for the evolution of hydride precipitation in zirconium. Part II: specimen with flaws. *J. Nucl. Mater.* **378**, 120–125 (2008).
87. Zhao, Z. et al. Characterization of zirconium hydrides and phase field approach to a mesoscopic-scale modeling of their precipitation. *J. ASTM Int.* **5**, 31–51 (2008).
88. Li, Y. L., Hu, S. Y., Zhang, L. & Sun, X. Non-classical nuclei and growth kinetics of Cr precipitates in FeCr alloys during aging. *Modelling Simul. Mater. Sci. Eng.* **22**, 025002 (2014).
89. Badillo, A., Bellon, P. & Averback, R. S. A phase field model for segregation and precipitation induced by irradiation in alloys. *Modelling Simul. Mater. Sci. Eng.* **23**, 035008 (2015).
90. Biner, S. B., Rao, W. F. & Zhang, Y. F. The stability of preprecipitates and the role of lattice defects in Fe-1at% Cu-1at% Ni-1at% Mn alloy: a phase-field model study. *J. Nucl. Mater.* **468**, 9–16 (2016).
91. Millett, P. C., Wolf, D., Desai, T., Rokkam, S. & El-Azab, A. Phase-field simulation of thermal conductivity in porous polycrystalline microstructures. *J. Appl. Phys.* **104**, 033512 (2008).
92. Ahmed, K., Pakarinen, J., Allen, T. & El-Azab, A. Phase field simulation of grain growth in porous uranium dioxide. *J. Nucl. Mater.* **446**, 90–99 (2014).
93. Tonks, M. R., Zhang, Y., Bai, X. & Millett, P. C. Demonstrating the temperature gradient impact on grain growth in uo2 using the phase field method. *Mater. Res. Lett.* **2**, 23–28 (2014).
94. Mei, Z. G. et al. Grain growth in U-7Mo alloy: a combined first-principles and phase field study. *J. Nucl. Mater.* **473**, 300–308 (2016).
95. Liang, L. et al. Mesoscale model for fission-induced recrystallization in U-7Mo alloy. *Comput. Mater. Sci.* **124**, 228–237 (2016).
96. Millett, P. C. & Tonks, M. Application of phase-field modeling to irradiation effects in materials. *Curr. Opin. Solid State Mater. Sci.* **15**, 125–133 (2011).
97. Hu, S. Y., Burkes, D., Lavender, C. A. & Joshi, V. Effect of grain morphology on gas bubble swelling in UMo fuels—a 3D microstructure dependent booth model. *J. Nucl. Mater.* **480**, 323–331 (2016).
98. Chang, K., Lee, G. G. & Kwon, J. A phase-field modeling of void swelling in the Austenitic stainless steel. *Radiat. Eff. Defects Solids* **171**, 242–251 (2016).
99. Welland, M. J., Lewis, B. J. & Thompson, W. T. A comparison of Stefan and phase field modeling techniques for the simulation of melting nuclear fuel. *J. Nucl. Mater.* **376**, 229–239 (2008).
100. Welland, M. J., Thompson, W. T., Lewis, B. J. & Manara, D. Computer simulations of non-congruent melting of hyperstoichiometric uranium dioxide. *J. Nucl. Mater.* **385**, 358–363 (2009).
101. Welland, M. J., Lewis, B. J. & Thompson, W. T. Review of high temperature thermochemical properties and application in phase-field modelling of incipient melting in defective fuel. *J. Nucl. Mater.* **412**, 342–349 (2011).
102. Tonks, M. R. et al. Fully-coupled engineering and mesoscale simulations of thermal conductivity in UO2 fuel using an implicit multiscale approach. *J. Phys. Conf. Ser.* **180**, 012078 (2009).
103. Millett, P. C. & Tonks, M. Meso-scale modeling of the influence of intergranular gas bubbles on effective thermal conductivity. *J. Nucl. Mater.* **412**, 281–286 (2011).
104. Li, D., Li, Y., Hu, S., Sun, X. & Khaleel, M. Predicting thermal conductivity evolution of polycrystalline materials under irradiation using multiscale approach. *Metall. Mater. Trans. A* **43A**, 1060–1069 (2012).
105. Chockalingam, K., Millett, P. C. & Tonks, M. R. Effects of intergranular gas bubbles on thermal conductivity. *J. Nucl. Mater.* **430**, 166–170 (2012).
106. Hu, S. Y., Casella, A., Lavender, C. A., Senor, D. J. & Burkes, D. Assessment of effective thermal conductivity in U-Mo metallic fuels with distributed gas bubbles. *J. Nucl. Mater.* **462**, 64–76 (2015).
107. Hu, S. Y., Li, Y. L., McCloy, J., Montgomery, R. & Henager, C. H. Magnetic hardening from the suppression of domain walls by nonmagnetic particles. *IEEE Magn. Lett.* **4**, 3500104 (2013).
108. Li, Y. L. et al. Computational and experimental investigations of magnetic domain structures in patterned magnetic thin films. *J. Phys. D-Appl. Phys.* **48**, 305001 (2015).
109. Ratsch, C. et al. Level-set method for island dynamics in epitaxial growth. *Phys. Rev. B* **65**, 195403 (2002).
110. Cahn, J. W. On spinodal decomposition. *Acta Metall. Mater.* **9**, 795–801 (1961).
111. Cahn, J. W. & Allen, S. M. A microscopic theory of domain wall motion and its experimental verification in Fe-Al alloy domain growth kinetics. *J. de Physique* **38**, C7–51 (1977).
112. Norgett, M. J., Robinson, M. T. & Torrens, I. M. Proposed method of calculating displacement dose-rates. *Nucl. Eng. Des.* **33**, 50–54 (1975).
113. Brailsford, A. D. & Bullough, R. The theory of sink strengths. *Philos. Trans. R. Soc. A* **302**, 87–137 (1981).
114. Phythian, W. J., Stoller, R. E., Foreman, A. J. E., Calder, A. F. & Bacon, D. J. A comparison of displacement cascades in copper and iron by molecular-dynamics and its application to microstructural evolution. *J. Nucl. Mater.* **223**, 245–261 (1995).
115. Bi, Z. Q. & Sekerka, R. F. Phase-field model of solidification of a binary alloy. *Physica. A* **261**, 95–106 (1998).
116. Elder, K. R., Grant, M., Provatas, N. & Kosterlitz, J. M. Sharp interface limits of phase-field models. *Phys. Rev. E* **64**, 021604 (2001).
117. Hohenberg, P. C. & Halperin, B. I. Theory of dynamic critical phenomena. *Rev. Mod. Phys.* **49**, 435–479 (1977).
118. Wheeler, A. A., Boettinger, W. J. & McFadden, G. B. Phase-field model for iso-thermal phase-transitions in binary-alloys. *Phys. Rev. A* **45**, 7424–7439 (1992).
119. Kim, S. G., Kim, W. T. & Suzuki, T. Phase-field model for binary alloys. *Phys. Rev. E* **60**, 7186–7197 (1999).
120. Chen, L. Q. & Yang, W. Computer-simulation of the domain dynamics of a quenched system with a large number of nonconserved order parameters—the grain-growth kinetics. *Phys. Rev. B* **50**, 15752–15756 (1994).
121. Abe, K., Masuyama, T., Satou, M. & Hamilton, M. L. Neutron-irradiation damage and void lattice formation in a molybdenum alloy TZM. *Mater. Trans. JIM* **34**, 1137–1142 (1993).
122. Jager, W. & Trinkaus, H. Defect ordering in metals under irradiation. *J. Nucl. Mater.* **205**, 394–410 (1993).
123. Ghoniem, N. M., Walgraef, D. & Zinkle, S. J. Theory and experiment of nanostructure self-organization in irradiated materials. *J. Comput.-Aided Mater. Des.* **8**, 1–38 (2001).

124. Gan, J. et al. Transmission electron microscopy characterization of irradiated U-7Mo/Al-2Si dispersion fuel. *J. Nucl. Mater.* **396**, 234–239 (2010).
125. Yu, H. C. & Lu, W. Dynamics of the self-assembly of nanovoids and nanobubbles in solids. *Acta Mater.* **53**, 1799–1807 (2005).
126. Opplestrup, T., Bulatov, V. V., Gilmer, G. H., Kalos, M. H. & Sadigh, B. First-passage Monte Carlo algorithm: diffusion without all the hops. *Phys. Rev. Lett.* **97**, 230602 (2006).
127. Schwen, D., Martinez, E. & Caro, A. On the analytic calculation of critical size for alpha prime precipitation in FeCr. *J. Nucl. Mater.* **439**, 180–184 (2013).
128. Novy, S., Pareige, P. & Pareige, C. Atomic scale analysis and phase separation understanding in a thermally aged Fe-20 at.%Cr alloy. *J. Nucl. Mater.* **384**, 96–102 (2009).
129. Finel, A., Le Bouar, Y., Gaubert, A. & Salman, U. Phase field methods: microstructures, mechanical properties and complexity. *C. R. Phys.* **11**, 245–256 (2010).
130. Klinsmann, M., Rosato, D., Kamlah, M. & McMeeking, R. M. An assessment of the phase field formulation for crack growth. *Comput. Meth. Appl. Mech. Eng* **294**, 313–330 (2015).
131. Kuhn, C., Schluter, A. & Muller, R. On degradation functions in phase field fracture models. *Comput. Mater. Sci.* **108**, 374–384 (2015).
132. Chakraborty, P., Zhang, Y. F. & Tonks, M. R. Multi-scale modeling of microstructure dependent intergranular brittle fracture using a quantitative phase-field based method. *Comput. Mater. Sci.* **113**, 38–52 (2016).
133. Kumar, A. & Garner, F. A. Saturation of proton-induced swelling in Aisi-316. *J. Nucl. Mater.* **117**, 234–238 (1983).
134. Straalsund, J. L., Powell, R. W. & Chin, B. A. An overview of neutron-irradiation effects in Imfbr materials. *J. Nucl. Mater.* **108**, 299–305 (1982).
135. Porollo, S. I. et al. Swelling and void-induced embrittlement of austenitic stainless steel irradiated to 73-82 dpa at 335-365 degrees C. *J. Nucl. Mater.* **263**, 1613–1617 (1998).
136. Vorobjev, A. N. et al. Irradiation creep and stress-enhanced swelling of Fe-16Cr-15Ni-Nb austenitic stainless steel in BN-350. *J. Nucl. Mater.* **263**, 1618–1622 (1998).
137. Surh, M. P., Sturgeon, J. B. & Wolfer, W. G. Vacancy cluster evolution and swelling in irradiated 316 stainless steel. *J. Nucl. Mater.* **328**, 107–114 (2004).
138. Dollins, C. C. & Ocken, H. Re-solution effects and fission gas swelling in UO₂. *J. Nucl. Mater.* **45**, 150–162 (1972).
139. Booth, A. H. A Method of Calculating Fission Gas Diffusion from UO₂ Fuel and its Application to the X-2-f Loop Test. Report No. AECL 496, (Atomic Energy Canada, 1957).
140. Mitra, A. et al. Magnetic evaluation of creep in modified 9Cr-1Mo steel. *Scr. Mater.* **57**, 813–816 (2007).
141. Kamada, Y. et al. Ion-irradiation enhancement of materials degradation in Fe-Cr single crystals detected by magnetic technique. *J. Nucl. Mater.* **442**, S861–S864 (2013).
142. Mohapatra, J. N. et al. Effect of Cr-rich phase precipitation on magnetic and mechanical properties of Fe-20% Cr alloy. *IEEE T Magn* **47**, 4356–4359 (2011).
143. Hubert, A. & Schaefer, R. *Magnetic Domain: the Analysis of Magnetic Microstructures*. (Springer, 1998).
144. Fu, H. H. et al. The Sunway Taihu Light supercomputer: system and applications. *Sci. China-Inf. Sci.* **59**, 16 (2016).



Open Access This article is licensed under a Creative Commons Attribution 4.0 International License, which permits use, sharing, adaptation, distribution and reproduction in any medium or format, as long as you give appropriate credit to the original author(s) and the source, provide a link to the Creative Commons license, and indicate if changes were made. The images or other third party material in this article are included in the article's Creative Commons license, unless indicated otherwise in a credit line to the material. If material is not included in the article's Creative Commons license and your intended use is not permitted by statutory regulation or exceeds the permitted use, you will need to obtain permission directly from the copyright holder. To view a copy of this license, visit <http://creativecommons.org/licenses/by/4.0/>.

© The Author(s) 2017